ARTICLES
https://doi.org/10.1038/s44161-022-00047-3
nature cardiovascular research

Check for updates

Endothelial plasticity drives aberrant vascularization and impedes cardiac repair after myocardial infarction

Menggui Huang[1,12], Fan Yang[1,12], Duo Zhang[1,12], Maohuan Lin[2,11,12], Hao Duan[1], Rakan El-Mayta[3], Lin Zhang[4], Ling Qin[5], Swapnil V. Shewale[6], Liming Pei[6,7], Michael J. Mitchell[3,6,8,9,10], Daniel J. Rader[2,6], Yi Fan[1,6,8,9,13] ✉ and Yanqing Gong[2,6,13] ✉

Myocardial infarction (MI) is a leading cause of death worldwide, largely because efficient interventions to restore cardiac function after MI are currently lacking. Here, we characterize vascular aberrancies induced by MI and propose to target acquired endothelial cell (EC) changes to normalize vessels and promote cardiac repair after MI. Single-cell transcriptome analyses of MI-associated ECs indicates that ECs acquire mesenchymal gene signatures that result in phenotypic and functional changes and lead to vessel abnormalities. We identify a platelet-derived growth factor (PDGF)–nuclear factor κB (NF-κB)–hypoxia-inducible factor 1-α (HIF-1α) axis that induces Snail expression and mesenchymal phenotypes in ECs under hypoxia, altogether causing aberrant vascularization. EC-specific knockout of platelet-derived growth factor receptor beta (PDGFR-β), pharmacological PDGFR inhibition or nanoparticle-based targeted PDGFR-β small interfering RNA delivery in mice attenuates vascular abnormalities in the infarcted tissue and improves cardiac repair after MI. These findings illustrate a mechanism controlling aberrant neovascularization after ischemia and suggest that targeting PDGF/Snail-mediated endothelial plasticity may offer opportunities for normalizing vasculature and treating ischemic heart diseases.

Acute MI is one of the leading causes of mortality and morbidity in humans worldwide. Formation of new blood vessels, that is, neovascularization, leads to blood reperfusion in the infarcted tissue, and is, therefore, fundamental to cardiac repair and function recovery after MI[1]. Therapeutic stimulation of neovascularization has been exploited in last three decades but the benefit has been small and transient in ischemic heart disease[2–6]. As a potential reason for insufficient recovery and therapeutic difficulties, newly formed vasculature under an ischemic condition, induced either intrinsically by hypoxia or therapeutically by pro-angiogenic factors, could be associated with vessel abnormalities, for example, tortuous structure with leakiness and excessive outgrowth and sprouting, which have been well characterized in cancer settings[7,8]; this may compromise vessel delivery function and likely impede cardiac repair after MI.

Cell plasticity in ECs has been well characterized during embryonic development[9,10]. In pathological settings including cardiac, renal and liver fibrosis, ossifying myositis, pulmonary hypotension and cerebral cavernous malformation, ECs can undergo endothelial–mesenchymal transition de novo to generate fibroblasts and stem-like cells[10–12]. Recent transcriptome analyses by multispectral endothelial lineage tracing show that mouse ECs exhibit a proliferative nature and undergo clonal expansion in the settings of MI; interestingly, these ECs express endothelial–mesenchymal transition markers in a time-dependent manner and acquire transient mesenchymal activation[13–15], suggesting that endothelial plasticity may be temporally associated with new vessel growth. In this study, we show that the MI-associated vasculature is characterized by prominent vessel abnormalities that are associated with robust endothelial plasticity toward a partial endothelial–mesenchymal transition. We reveal that ECs acquire PDGF/Snail-mediated genetic programming to induce mesenchymal activation but retain endothelial identity and functions, enhancing cell proliferation and migration and disrupting cell–cell adhesion, leading to aberrant neovascularization. Our study suggests that vessel normalization by targeting PDGF-dependent endothelial plasticity may provide a promising strategy for treating ischemic heart disease.

Results

MI is associated with aberrant vascularity. We initially took advantage of a light sheet fluorescence imaging system to analyze vessel function and structure at the whole-organ-level with *Cdh5-Cre*^{ERT2};*Rosa-LSL-tdTomato* mice where tdTomato expression is driven by the EC-specific promoter *Cdh5*. MI was induced by ligation of the left anterior descending (LAD) coronary artery,

[1]Department of Radiation Oncology, University of Pennsylvania Perelman School of Medicine, Philadelphia, PA, USA. [2]Division of Human Genetics and Translational Medicine, Department of Medicine, University of Pennsylvania Perelman School of Medicine, Philadelphia, PA, USA. [3]Department of Bioengineering, University of Pennsylvania School of Engineering and Applied Science, Philadelphia, PA, USA. [4]Department of Obstetrics & Gynecology, University of Pennsylvania Perelman School of Medicine, Philadelphia, PA, USA. [5]Department of Orthopaedic Surgery, University of Pennsylvania Perelman School of Medicine, Philadelphia, PA, USA. [6]Cardiovascular Institute, University of Pennsylvania Perelman School of Medicine, Philadelphia, PA, USA. [7]Center for Mitochondrial and Epigenomic Medicine, Department of Pathology and Laboratory Medicine, Children's Hospital of Philadelphia, Philadelphia, PA, USA. [8]Abramson Cancer Center, University of Pennsylvania Perelman School of Medicine, Philadelphia, PA, USA. [9]Institute for Immunology, University of Pennsylvania Perelman School of Medicine, Philadelphia, PA, USA. [10]Institute for Regenerative Medicine, University of Pennsylvania Perelman School of Medicine, Philadelphia, PA, USA. [11]Present address: Department of Cardiology, Sun Yat-sen Memorial Hospital, Sun Yat-sen University, Guangzhou, China. [12]These authors contributed equally: Menggui Huang, Fan Yang, Duo Zhang, Maohuan Lin. [13]These authors jointly supervised this work: Yi Fan, Yanqing Gong. ✉e-mail: fanyi@upenn.edu; gongy@pennmedicine.upenn.edu

followed by lectin perfusion. Strikingly, our analysis revealed that the vasculature in the MI area, albeit robustly formed particularly in the board zone, was poorly perfused (Fig. 1a,b) and exhibited a chaotic structure, showing an undefined vascular hierarchy (Fig. 1c) with reduced vessel diameter and enhanced branching (Fig. 1d). Moreover, immunofluorescence analysis showed that capillary ECs in MI tissue exhibited an abnormal structure, with a tortuous and disorganized morphology, compared to well-organized vasculature in a normal left ventricle (LV) (Extended Data Fig. 1a). In accordance with these findings, MI-associated vasculature showed reduced coverage with NG-2$^+$ pericytes and collagen IV, suggesting vessel lack of maturation in infarcted tissue (Extended Data Fig. 1b,c). These results indicate functional and structural abnormalities in MI-associated vasculature.

Robust endothelial plasticity in MI-associated ECs. To explore the mechanism underlying vascular aberrancy, we investigated transcriptome alteration in MI-associated ECs by single-cell RNA sequencing (scRNA-seq) analysis of *Cdh5-Cre*^{ERT2};*Rosa-LSL-tdTomato* mice (Fig. 1e). Nonlinear dimensionality reduction by uniform manifold approximation and projection (UMAP) analysis of the whole transcriptome gene signature assigned single cells into several transcriptionally distinct clusters (Fig. 1f), with tdTomato$^+$ EC-derived cells identified and characterized as vascular endothelial cadherin (VE-cadherin)$^+$, vascular endothelial growth factor receptor 2 (VEGFR2)$^+$ and CD31$^+$ cells (Fig. 1g–i). Notably, tdTomato$^+$ ECs expressed the mesenchymal-associated markers α-smooth muscle actin (α-SMA, *Acta2*), neural cadherin (N-cadherin) (*Cdh2*), collagen 1 (*Col1a1* and *Col1a2*), fibronectin (*Fn1*), PDGFR-β (*Pdgfrb*), fibroblast-specific protein-1 (FSP1) (*S100a4*), CD90 (*Thy1*) and *Zeb2* in a time-dependent manner, reaching peaks at week 1 after MI with 20–70% of ECs expressing these mesenchymal genes, followed by a gradual decrease (Fig. 1i). Interestingly, compared with the expression of mesenchymal genes, such as *Acta2*, *S100a4* and *Col1a1*, in a small portion (1–3%) of control normal cardiac ECs, 5–20% MI ECs collected 3 or 8 weeks after MI still expressed some of these genes, suggesting a low-level mesenchymal activation retained for 8 weeks, after a transient and robust activation in the first week (Fig. 1i). Furthermore, pseudotime analysis verified time-dependent cell plasticity in these cells (Fig. 1j) and interestingly showed time-dependent courses of α-SMA and PDGFR-β expression, which peaked at week 1 after MI and was sustained in a small cell population during weeks 2–8 after MI, while a small portion of ECs progressed toward expression reduction of the EC-specific gene *Cdh5* (VE-cadherin) during 1–8 weeks after MI (Fig. 1k), suggesting a temporally regulated trajectory of EC lineage progress to mesenchymal states. Consistent with these findings, a certain population of ECs in the MI area, but not normal ECs, expressed the mesenchymal protein FSP1 (Fig. 2a).

ECs acquire mesenchymal phenotypes under MI conditions. Considering that tumor ECs undergo endothelial–mesenchymal transition via cell plasticity to enhance cell proliferation and migration and reduce cell–cell adhesion[16,17], our findings suggest that ECs may acquire similar mesenchymal phenotypes to induce vessel abnormalities after MI. To test this, the effects of cardiac-conditioned medium (CCM) on mesenchymal gene expression and cell functions were analyzed in normal cardiac microvascular ECs. CCM was collected from the culture medium of mouse cardiac HL-1 myocytes and primary cardiac fibroblasts under hypoxia. Exposure of ECs to CCM induced increases in FSP1 and α-SMA expression under hypoxia, or to a lesser extent, under normoxia (Fig. 2b). Similar effects were induced by treatment with CCM collected from primary mouse cardiomyocytes (Extended Data Fig. 2). Furthermore, immunofluorescence analysis showed that CCM induced FSP1 expression in >30% of ECs under hypoxia and caused a cell morphology shift from the characteristic cobblestone appearance to fibroblast-like, spindle-shaped cells with spikes (Fig. 2c), suggesting a potential lineage alteration. However, these treated cells still expressed VEGFR2 (Fig. 2b) and were able to uptake acetylated low-density lipoprotein (Ac-LDL), which acts as a proxy and functional readout for ECs (Fig. 2c), suggesting that key endothelial identity and function are retained in these treated cells, even after ECs acquire a mesenchymal gene signature. Furthermore, CCM maintained or stimulated cell proliferation under hypoxia (Fig. 2d), increased cell migration (Fig. 2e) and enhanced monolayer permeability (Fig. 2f). Together, these data suggest that ECs acquire mesenchymal phenotypes to induce vessel abnormalities under MI conditions.

Robust endothelial plasticity after MI. To explore the regulatory mechanism that controls EC plasticity, we performed bulk deep RNA-seq in sorted ECs derived from MI and healthy LV tissues, based on *Tie2-Cre*;*Rosa-LSL-tdTomato*-mediated endothelial lineage tracing. Bearing in mind that non-EC myeloid cells may also express Tie2[18], we sorted tdTomato$^+$F4/80$^-$ cells by flow cytometry to exclude an F4/80$^+$ macrophage population (Fig. 3a). The amount of yielded RNA (0.5–5.0 ng per mouse from sorted F4/80$^-$tdTomato$^+$ cells) was not sufficient for conventional RNA-seq analysis; thus, the extracted RNA underwent linear RNA amplification before RNA-seq. Dimensionality reduction by principal component analysis of gene expression showed a lineage switch in MI-associated ECs compared to normal ECs (Fig. 3b). Global analysis of the whole transcriptome indicated an increase in expression of about 1/4 of all genes as well as a decrease in expression of fewer genes (Fig. 3c,d). Interestingly, RNA-seq analysis showed upregulation (greater than tenfold) of mesenchymal genes including *S100a4* (FSP1), *Acta2* (α-SMA), *Cdh2* (N-cadherin), *Pdgfra/b* (PDGFR-α/β) and *Met* (c-Met) in MI ECs, compared with normal ECs (Fig. 3e); upregulated expression of *S100a4* and *Acta2* was verified by PCR with reverse transcription (RT–PCR) analysis (Extended Data Fig. 3). These findings confirm robust endothelial plasticity to acquire mesenchymal-like transcriptional activation in MI ECs.

PDGF induces mesenchymal-like activation under hypoxia. We analyzed the upregulated genes identified by RNA-seq in MI ECs. Our results showed that about 14% of these genes were

Fig. 1 | scRNA-seq analysis reveals dynamic endothelial plasticity in MI tissue, which is associated with vessel aberrancy. *Cdh5-Cre*^{ERT2};*LSL-tdTomato* mice underwent MI surgery or sham operation. **a**–**d**, Mice were perfused intravenously with DyLight 649-conjugated lectin three weeks after surgery; hearts were analyzed by light sheet fluorescence imaging. **a**, Whole-heart imaging representative images. The grid indicates 1 mm. **b**, Whole-heart imaging quantitative results for lectin perfusion in the MI area or corresponding normal LV region ($n = 3$ mice, mean ± s.e.m.). Statistical analysis by two-tailed Student's *t*-test. **c**, Imaging at MI area or corresponding normal LV region. Representative images. The grid indicates 500 μm. **d**, Imaging at MI area or corresponding normal LV region. Quantitative results for vessel diameter and branching ($n = 3$ mice, mean ± s.e.m.). Statistical analysis by two-tailed Student's *t*-test (top) and two-way ANOVA (bottom). a.u., arbitrary unit. **e**–**k**, Cells derived from MI or LV tissue were analyzed by scRNA-seq. **e**, Schematic approach. **f**,**g**, UMAP analysis of transcriptome gene signature in all cells (**f**) and tdTomato$^+$ cells (**g**). **h**, UMAP analysis of tdTomato$^+$ cells. **i**, Expression of EC markers and mesenchymal genes in tdTomato$^+$ cells. **j**,**k**, TdTomato$^+$ cells underwent pseudotime analysis. **j**, Cells underwent cell trajectory construction. **k**, Gene expression kinetics as a function of pseudotime. The arrows indicate cell populations that expressed the mesenchymal genes *Acta2* and *Pdgfrb*.

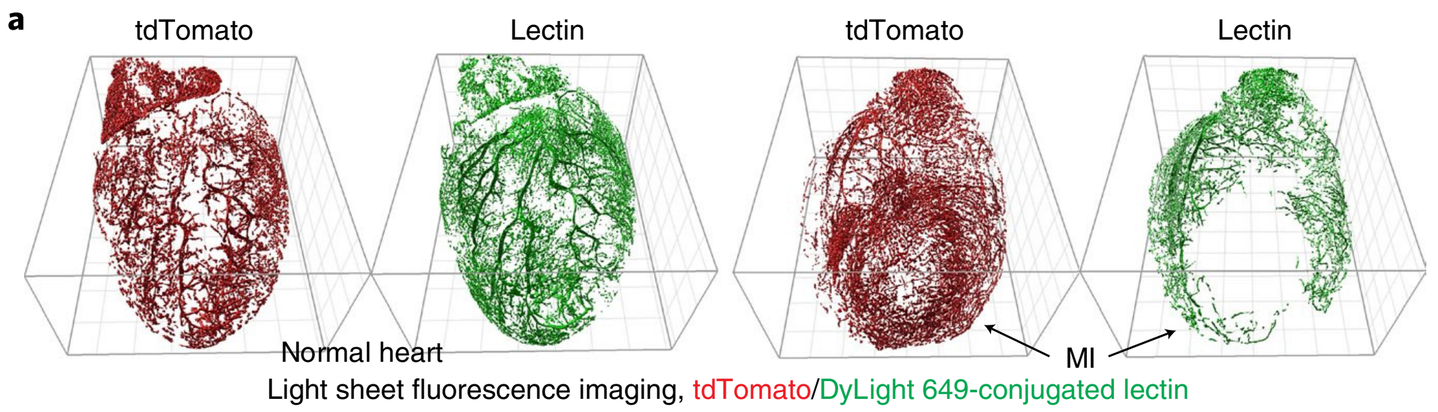
a
tdTomato
Lectin
tdTomato
Lectin
Normal heart
MI
Light sheet fluorescence imaging, tdTomato/DyLight 649-conjugated lectin

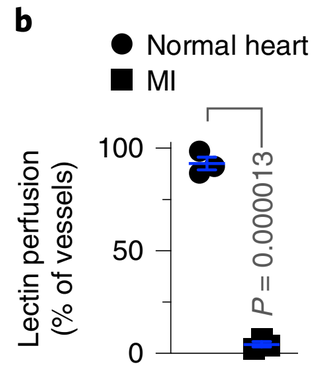
b
Normal heart
MI
Lectin perfusion (% of vessels)
100
50
0
P = 0.000013

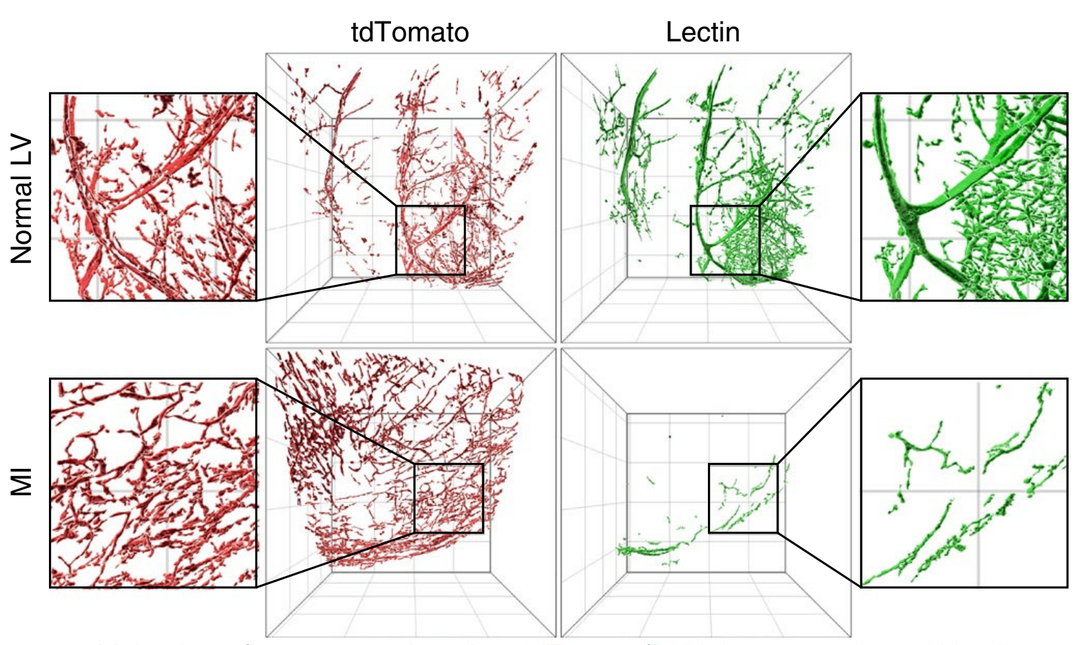
c
tdTomato
Lectin
Normal LV
MI
Light sheet fluorescence imaging, tdTomato/DyLight 649-conjugated lectin

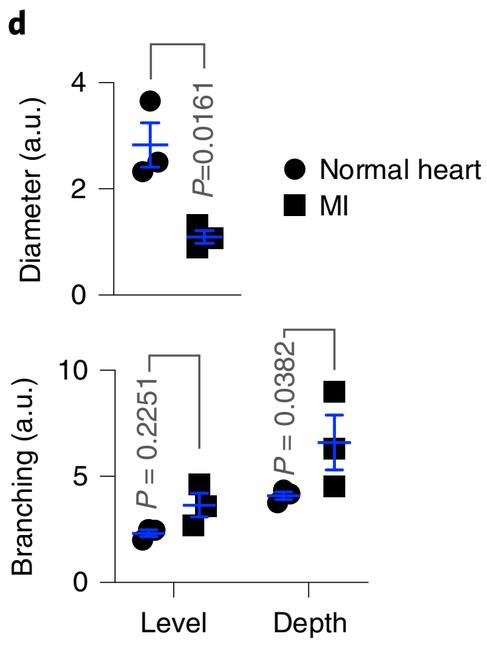
d
Diameter (a.u.)
4
2
0
P=0.0161
Normal heart
MI
Branching (a.u.)
10
5
0
P = 0.2251
P = 0.0382
Level
Depth

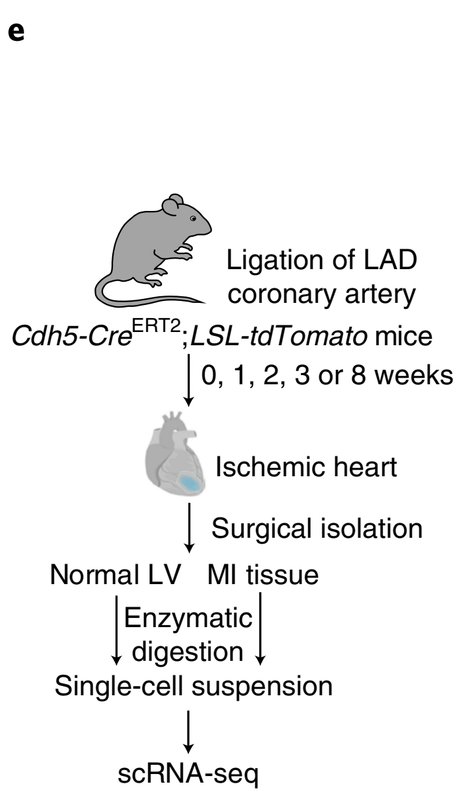
e
Ligation of LAD coronary artery
Cdh5-CreERT2;LSL-tdTomato mice
0, 1, 2, 3 or 8 weeks
Ischemic heart
Surgical isolation
Normal LV
MI tissue
Enzymatic digestion
Single-cell suspension
scRNA-seq

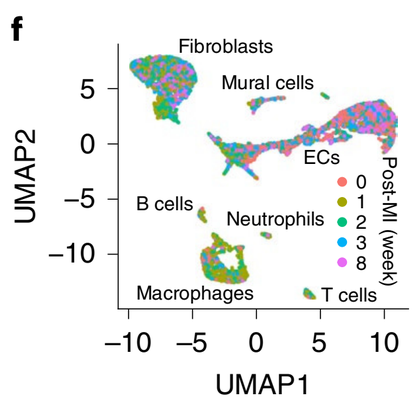
f
Fibroblasts
Mural cells
ECs
B cells
Neutrophils
Macrophages
T cells
Post-MI (week)
0
1
2
3
8
UMAP2
UMAP1

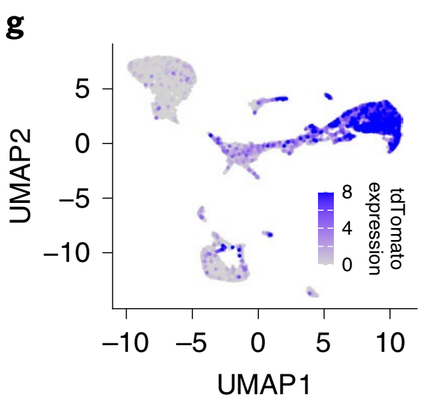
g
UMAP2
UMAP1
tdTomato expression
8
4
0

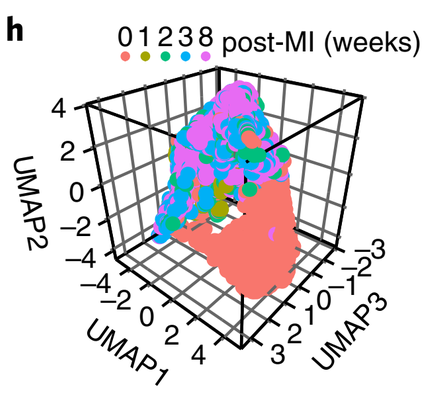
h
0 1 2 3 8 post-MI (weeks)
UMAP2
UMAP1
UMAP3

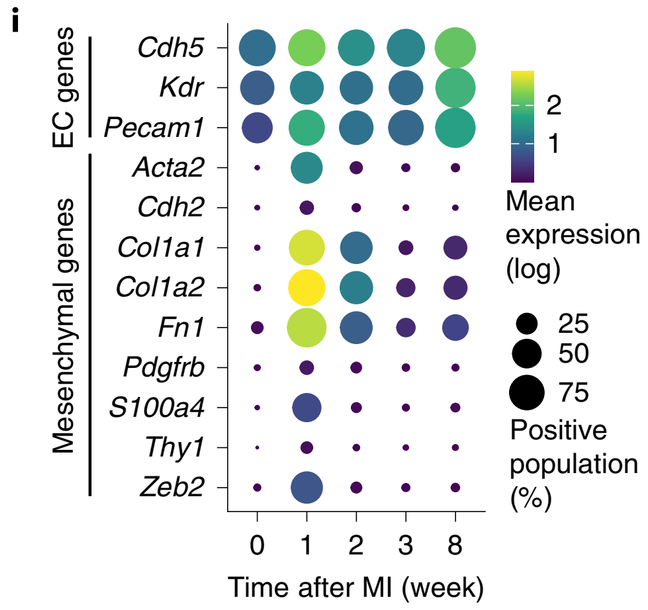
i
EC genes
Cdh5
Kdr
Pecam1
Mesenchymal genes
Acta2
Cdh2
Col1a1
Col1a2
Fn1
Pdgfrb
S100a4
Thy1
Zeb2
Mean expression (log)
2
1
Positive population (%)
25
50
75
0 1 2 3 8
Time after MI (week)

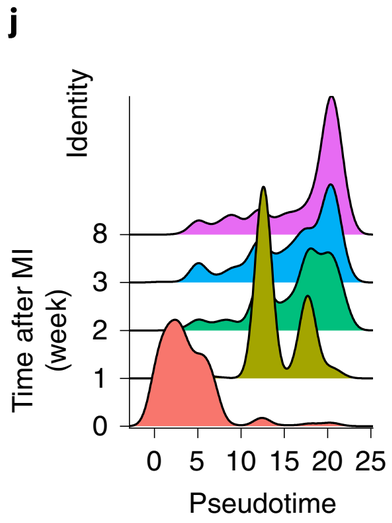
j
Identity
Time after MI (week)
8
3
2
1
0
0 5 10 15 20 25
Pseudotime

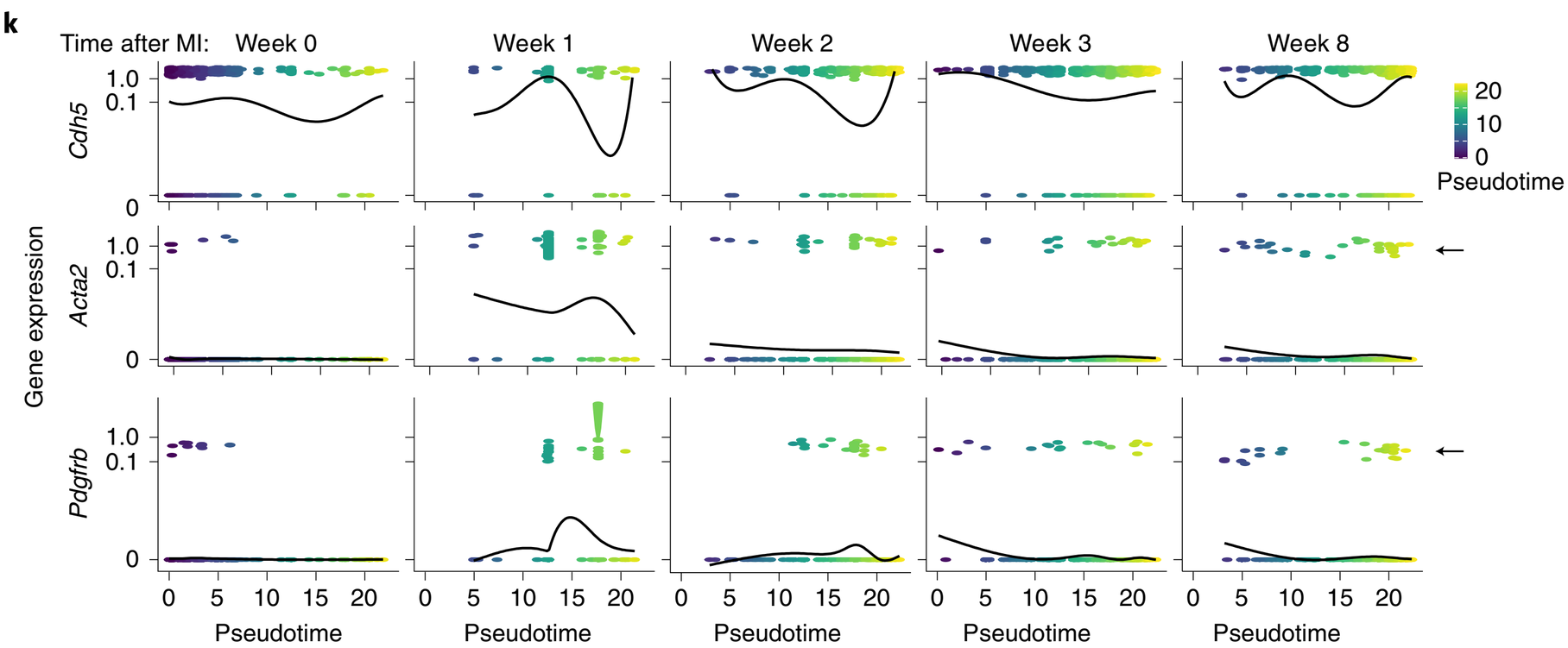
k
Time after MI: Week 0
Week 1
Week 2
Week 3
Week 8
Cdh5
Acta2
Pdgfrb
1.0
0.1
0
Gene expression
0 5 10 15 20
Pseudotime
20
10
0
Pseudotime

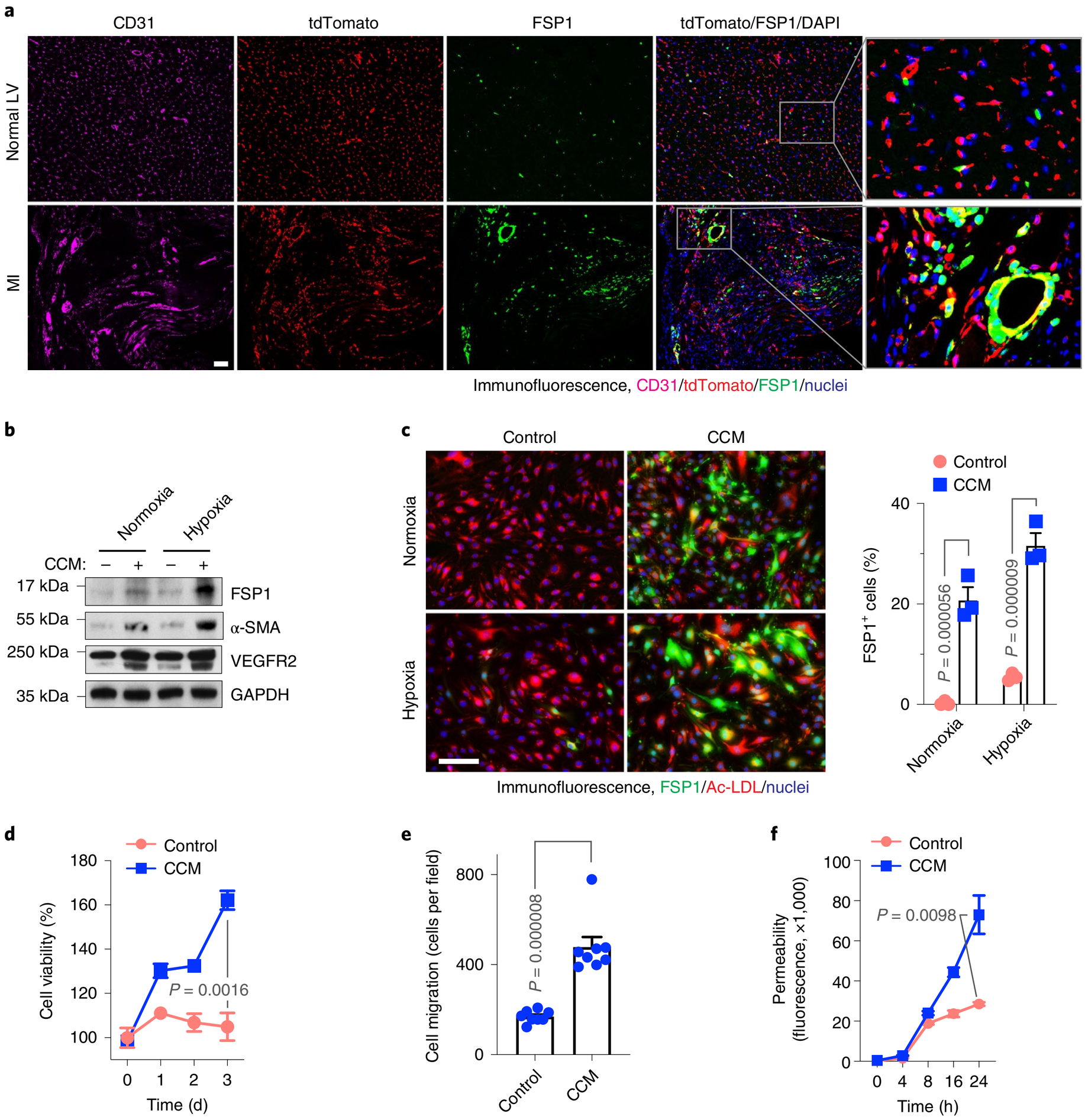

Fig. 2 | ECs acquire mesenchymal phenotypes under MI conditions. a, *Cdh5-Cre*^{ERT2}*;LSL-tdTomato* mice underwent MI surgery or sham operation. Hearts were excised three weeks after surgery. Tissue sections were immunostained with anti-FSP1 and anti-CD31 antibodies. Representative images in the normal LV and infarct zone are shown ($n=3$ mice). Mouse cardiac ECs were treated with CCM under normoxia or hypoxia for 2 d and cultured in normal medium. Bars indicate 100 μm. **b**–**f**, Mouse CCM was collected from primary cardiac fibroblasts and HL-1 cardiomyocytes cultured under hypoxia (1% O_2). **b**, EC lysates were immunoblotted. This experiment was repeated independently twice with similar results. **c**, ECs were incubated with Dil-Ac-LDL, followed by immunofluorescence analysis with anti-FSP1 antibody. Left: Representative images. The bar indicates 50 μm. Right: Quantified results ($n=3$ EC samples, mean ± s.e.m.). Statistical analysis by two-way ANOVA. **d**, EC viability under hypoxia was determined by cell viability analysis ($n=3$ EC samples, mean ± s.e.m.). Statistical analysis by two-tailed Student's *t*-test. **e**, EC migration was analyzed using Transwells ($n=8$ EC samples, mean ± s.e.m.). Statistical analysis by two-tailed Student's *t*-test. **f**, EC monolayer permeability was analyzed by measuring the fluorescence of diffused FITC-dextran across the Transwell membrane ($n=3$ EC samples, mean ± s.e.m.). Statistical analysis by two-tailed Student's *t*-test.

associated with pathway regulation; further gene ontology (GO) and pathway enrichment analysis identified the top regulated pathways including stem cell factor (SCF)-KIT, PDGF and c-Met (Fig. 3f). Among the ligands including SCF, PDGF and hepatocyte growth factor (HGF) that activate these pathways, PDGF-AB induced the most robust expression of FSP1, α-SMA and N-cadherin in ECs (Extended Data Fig. 4). Consistently, our RNA-seq analysis of MI ECs revealed a marked increase in expression of PDGF pathway-associated genes (Fig. 3g). Based on these findings, we focused our studies on the PDGF-mediated mechanism. PDGF is a dimeric glycoprotein that consists of two A subunits (PDGF-AA), two B subunits (PDGF-BB) or one of each (PDGF-AB)[19]. We tested the effects of these ligands on mesenchymal-like transcriptional activation. Our data showed PDGF-AB-induced expression of FSP1, α-SMA and N-cadherin in human cardiac microvascular ECs, particularly under hypoxia (Fig. 3h). Furthermore, pharmacological inhibition of PDGFR with crenolanib or small interfering RNA (siRNA)-mediated PDGFR-β knockdown abrogated CCM-induced FSP1 and α-SMA expression (Fig. 3i,j). Likewise, PDGFR-β knockdown reduced CCM-stimulated EC survival and proliferation under hypoxia (Fig. 3k) and attenuated CCM-induced EC migration (Fig. 3l). These findings suggest a critical role of PDGF for mesenchymal transcriptional activation and dysfunction in ECs under MI conditions.

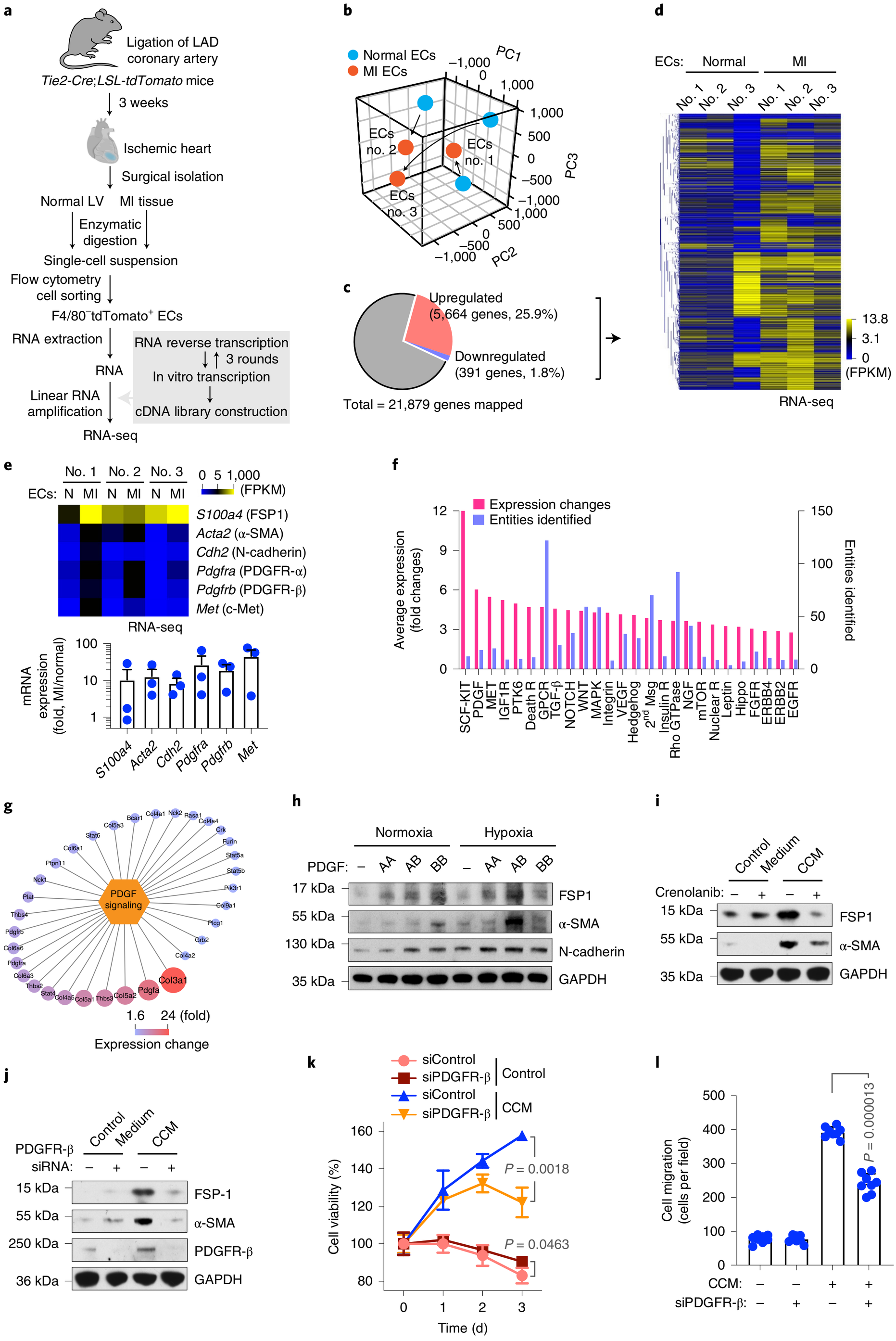
a
Ligation of LAD coronary artery
Tie2-Cre;LSL-tdTomato mice
3 weeks
Ischemic heart
Surgical isolation
Normal LV
MI tissue
Enzymatic digestion
Single-cell suspension
Flow cytometry cell sorting
F4/80⁻tdTomato⁺ ECs
RNA extraction
RNA
Linear RNA amplification
RNA reverse transcription
3 rounds
In vitro transcription
cDNA library construction
RNA-seq
b
Normal ECs
MI ECs
PC1
PC2
PC3
ECs no. 1
ECs no. 2
ECs no. 3
c
Upregulated (5,664 genes, 25.9%)
Downregulated (391 genes, 1.8%)
Total = 21,879 genes mapped
d
ECs: Normal MI
No. 1 No. 2 No. 3 No. 1 No. 2 No. 3
13.8
3.1
0
(FPKM)
RNA-seq
e
No. 1 No. 2 No. 3
ECs: N MI N MI N MI
0 5 1,000 (FPKM)
S100a4 (FSP1)
Acta2 (α-SMA)
Cdh2 (N-cadherin)
Pdgfra (PDGFR-α)
Pdgfrb (PDGFR-β)
Met (c-Met)
RNA-seq
mRNA expression (fold, MI/normal)
S100a4 Acta2 Cdh2 Pdgfra Pdgfrb Met
f
Expression changes
Entities identified
Average expression (fold changes)
Entities identified
SCF-KIT PDGF MET IGF1R PTK6 Death R GPCR TGF-β NOTCH WNT MAPK Integrin VEGF Hedgehog 2nd Msg Insulin R Rho GTPase NGF mTOR Nuclear R Leptin Hippo FGFR ERBB4 ERBB2 EGFR
g
PDGF signaling
Col3a1
Pdgfa
1.6 24 (fold)
Expression change
h
Normoxia Hypoxia
PDGF: – AA AB BB – AA AB BB
17 kDa FSP1
55 kDa α-SMA
130 kDa N-cadherin
35 kDa GAPDH
i
Control Medium CCM
Crenolanib: – + – +
15 kDa FSP1
55 kDa α-SMA
35 kDa GAPDH
j
Control Medium CCM
PDGFR-β siRNA: – + – +
15 kDa FSP-1
55 kDa α-SMA
250 kDa PDGFR-β
36 kDa GAPDH
k
siControl
siPDGFR-β
Control
siControl
siPDGFR-β
CCM
Cell viability (%)
Time (d)
P = 0.0018
P = 0.0463
l
Cell migration (cells per field)
P = 0.000013
CCM: – – + +
siPDGFR-β: – + – +

Fig. 3 | Linear RNA amplification and transcriptome analysis identifies PDGF as a critical regulator of endothelial plasticity and dysfunction under MI. **a**–**g**, MI was induced in *Tie2-Cre;LSL-tdTomato* mice. ECs were isolated from mouse normal LV and MI tissues. RNA was extracted and underwent linear amplification and RNA-seq analysis ($n=3$ mice). **a**, Experimental procedure. **b**, All mapped genes were analyzed by principal component analysis. **c**,**d**, Genes with an average expression change >60% were identified. **c**, Global transcriptome gene expression changes. **d**, Heatmap of clustered genes with changed expression. FPKM, fragments per kilobase of transcript per million mapped reads. **e**, Fold of mesenchymal gene expression in MI-associated ECs compared to normal ECs. Top: Heatmap. Bottom: Quantified results ($n=3$ mice, mean ± s.e.m.). **f**, Bioinformatic analysis of upregulated genes in MI-associated ECs. GO and pathway set analysis of upregulated genes. **g**, Identified upregulated genes in the PDGF pathway. **h**, Human cardiac microvascular ECs were treated with 100 ng ml^{-1} PDGF-AA, PDGF-AB or PDGF-BB under normoxia or hypoxia. Cell lysates underwent immunoblotting. **i**, Mouse cardiac microvascular ECs pretreated with crenolanib or control 0.1% dimethylsulfoxide (DMSO) were incubated with CCM or control medium for 2 d. Cell lysates underwent immunoblotting. **j**–**l**, Mouse cardiac ECs were treated with siRNA targeting PDGFR-β or control scrambled sequence, followed by incubation with CCM or control medium for 2 d. **j**, EC lysates underwent immunoblotting. **h**–**j**, These experiments were repeated independently twice with similar results. **k**,**l**, ECs were cultured back in normal medium. **k**, Cell viability under hypoxia was determined ($n=3$ EC samples, mean ± s.d.). Statistical analysis by two-tailed Student's *t*-test. **l**, Cell migration was analyzed with a Transwell ($n=8$ EC samples, mean ± s.d.). Statistical analysis by two-tailed Student's *t*-test.

PDGF activates NF-kB–HIF1-α–Snail. Epithelial–mesenchymal transition, a similar cellular process to endothelial plasticity, has been well characterized as mediated through multiple transcription factors including Snail, Slug, transcription factor 3 (TCF3), Twist-related protein 1 (TWIST1) and TWIST2 and zinc finger E-box-binding homeobox 1 (ZEB1) and ZEB2 (refs. [20–22]). We analyzed their expression in MI-associated ECs. RNA-seq analysis revealed robust expression of Snail, Slug, TWIST1, ZEB1 and ZEB2 in MI ECs, particularly showing an increase in Snail expression, compared with the corresponding normal ECs (Fig. 4a). Upregulated expression of Snail and TWIST1 in MI ECs was verified by RT–PCR analysis (Extended Data Fig. 3). Interestingly, PDGF-AB selectively upregulated expression of Snail but not Slug, TCF3, ZEB1 or SIP1 expression under hypoxia in human cardiac ECs (Fig. 4b), suggesting a potential role of Snail in EC plasticity. Likewise, siRNA-mediated *Snail* knockdown abrogated PDGF-AB-induced FSP1 expression in ECs (Fig. 4c), indicating that PDGF induces mesenchymal transcriptional activation through Snail.

We investigated the mechanism for PDGF-induced Snail expression. Our multiplex transcription factor activity analysis showed that PDGF-AB activates several transcription factors, with the top five including NF-κB, serum response factor, signal transducer and activator of transcription 3 (STAT3), myoblast determination protein 1 and transcription factor NRF1 in cardiac ECs, while PDGF-AB or hypoxia reduced the DNA-binding activities of most other tested transcription factors (Fig. 4d). Like our previous work showing that PDGF-AB activates the NF-κB signaling pathway in brain tumor ECs[23], siRNA-mediated NF-κB knockdown abrogated PDGF-AB-induced Snail and FSP1 expression under hypoxia, and to a lesser extent, under normoxia (Fig. 4e). HIF1-α is a master transcription factor that regulates hypoxia-induced cellular processes. Interestingly, PDGF-AB stimulated HIF1-α messenger RNA and protein expression in ECs (Fig. 4e,f). Moreover, siRNA-mediated HIF1-α knockdown inhibited PDGF-AB-induced Snail and FSP1 expression under hypoxia (Fig. 4g), suggesting a critical role of HIF1-α for PDGF-induced mesenchymal transcriptional activation in addition to NF-κB. Notably, NF-κB knockdown inhibited PDGF-AB-induced HIF1-α expression under normoxia and hypoxia (Fig. 4e,f), suggesting that PDGF-AB activates NF-κB to induce HIF1-α expression. Furthermore, chromatin immunoprecipitation (ChIP) analysis showed that both NF-κB and HIF1-α were able to bind to the Snail promoter in a PDGF-inducible manner (Fig. 4h–j). Together, these findings suggest that PDGF activates NF-κB to induce Snail expression; in addition, NF-κB-mediated HIF1-α transcription further enhances Snail expression under hypoxia.

PDGF/Snail suppresses VE-cadherin expression under hypoxia. A hallmark of epithelial–mesenchymal transition is the downregulation of E-cadherin by transcriptional repression to reinforce the destabilization of adherens junctions in epithelial cells[22]. Our data show that PDGF-AB robustly downregulates VE-cadherin expression under hypoxia in ECs (Fig. 5a). Moreover, Snail knockdown rescued VE-cadherin expression in PDGF-AB-treated ECs under hypoxia (Fig. 5b). Consistent with the critical role of Snail for VE-cadherin downregulation, PDGF-AB induced Snail binding to the VE-cadherin promoter (Fig. 5c), collectively suggesting that Snail binds to the VE-cadherin promoter and suppresses its expression in a PDGF-inducible mechanism in ECs. To determine the contribution of this mechanism to EC plasticity and cell functions, VE-cadherin was enforced to reexpress in PDGF-treated ECs by lentiviral transduction with active CRISPR/single-guide RNA (sgRNA) (Fig. 5d). Reexpression of VE-cadherin inhibited expression of the mesenchymal proteins FSP1 and N-cadherin (Fig. 5d) and attenuated cell proliferation (Fig. 5e) and monolayer permeability (Fig. 5f) induced by PDGF treatment under hypoxia. Together, these results identify a PDGF-AB–NF-κB–HIF1-α–Snail-mediated signaling axis that suppresses VE-cadherin expression and induces endothelial plasticity in an ischemic setting, by which enhanced EC

Fig. 4 | PDGF regulates EC plasticity under hypoxia via NF-κB- and HIF1-α-dependent Snail expression. **a**, ECs were isolated from normal mouse LV and MI tissues and underwent RNA-seq analysis. Gene expression of epithelial–mesenchymal transition-related transcription factors was determined. Upper: Heatmap. Bottom: Quantified results ($n=3$ mice, mean ± s.e.m.). **b**, Human cardiac microvascular ECs were treated with 100 ng ml^{-1} PDGF-AA, PDGF-AB or PDGF-BB under normoxia or hypoxia. Cell lysates underwent immunoblotting. **c**, Human ECs were transfected with siRNA targeting Snail or the control scrambled sequence, followed by treatment with PDGF-AB. Cell lysates underwent immunoblotting. **b**,**c**, These experiments were repeated independently twice with similar results. **d**, Human ECs were treated with PDGF-AB under normoxia or hypoxia, followed by multiplex transcriptional activity assay. **e**,**f**, Human ECs were pretreated with siRNA targeting NF-κB or the control sequence and incubated with PDGF-AB under normoxia or hypoxia. **e**, Cell lysates underwent immunoblotting. This experiment was repeated independently twice with similar results. **f**, RNA was analyzed by RT–PCR. Results were normalized with GAPDH levels ($n=3$ EC samples, mean ± s.e.m.). Statistical analysis by two-way ANOVA. **g**, Human ECs were pretreated with siRNA targeting HIF1-α or the control sequence and incubated with PDGF-AB under normoxia or hypoxia. Cell lysates underwent immunoblotting. This experiment was repeated independently twice with similar results. **h**–**j**, ChIP analysis. **h**, Primer information. Human ECs were treated with PDGF-AB under normoxia (**i**) or hypoxia (**j**), followed by ChIP analysis with different Snail primers after immunoprecipitation with anti-NF-kB (**i**) or anti-HIF1-α antibody ($n=3$ EC samples, mean ± s.e.m.) (**j**). TSS, transcription start site. Statistical analysis by two-tailed Student's *t*-test (**i**) or two-way ANOVA (**j**).

motility and proliferation, as well as disrupted cell–cell adhesion, lead to vascular aberrancy (Fig. 5g).

PDGFR-β knockout in ECs normalizes neovasculature after MI. We next tested the in vivo role of PDGF-mediated endothelial plasticity in cardiac repair and function recovery after MI. We generated EC-specific PDGFR-β knockout mice by crossing *Pdgfrb*$^{loxP/loxP}$ mice with *Cdh5-Cre*^{ERT2} mice (Fig. 6a). PDGFR-β was selected as the target because of its well-established developmental role for blood vessel formation and early hematopoiesis, while PDGFR-α signaling is critical for gastrulation and the development of the cranial and cardiac neural crest, gonads and other organs[19]. Efficient EC-specific

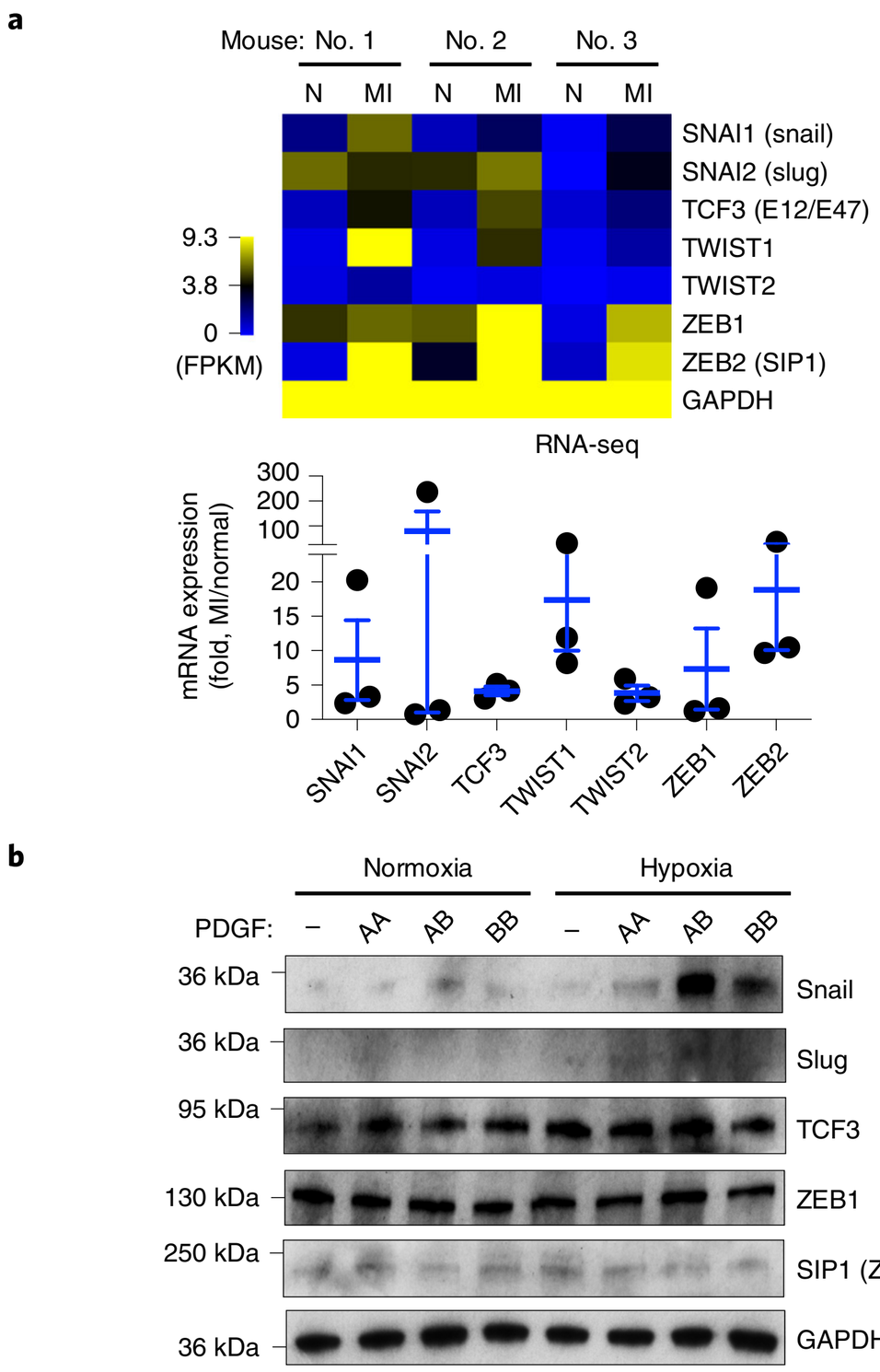

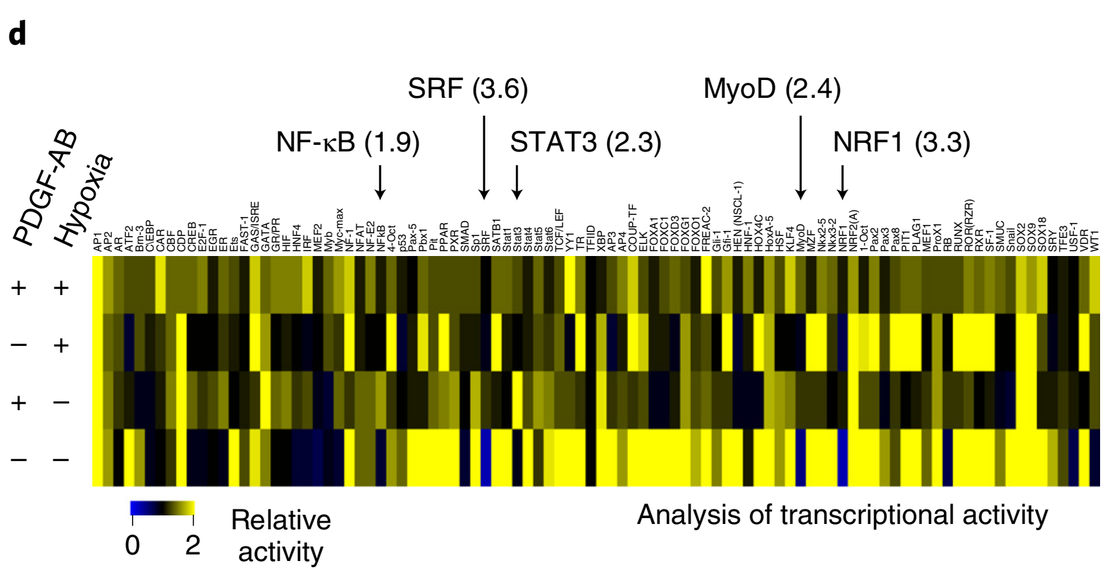

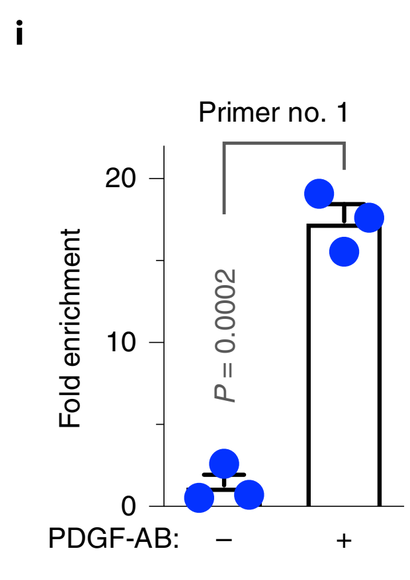

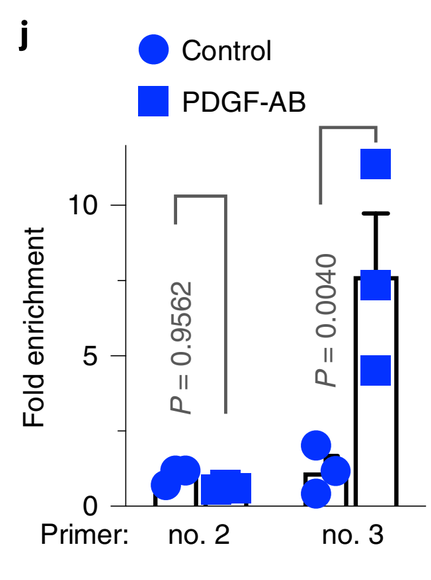

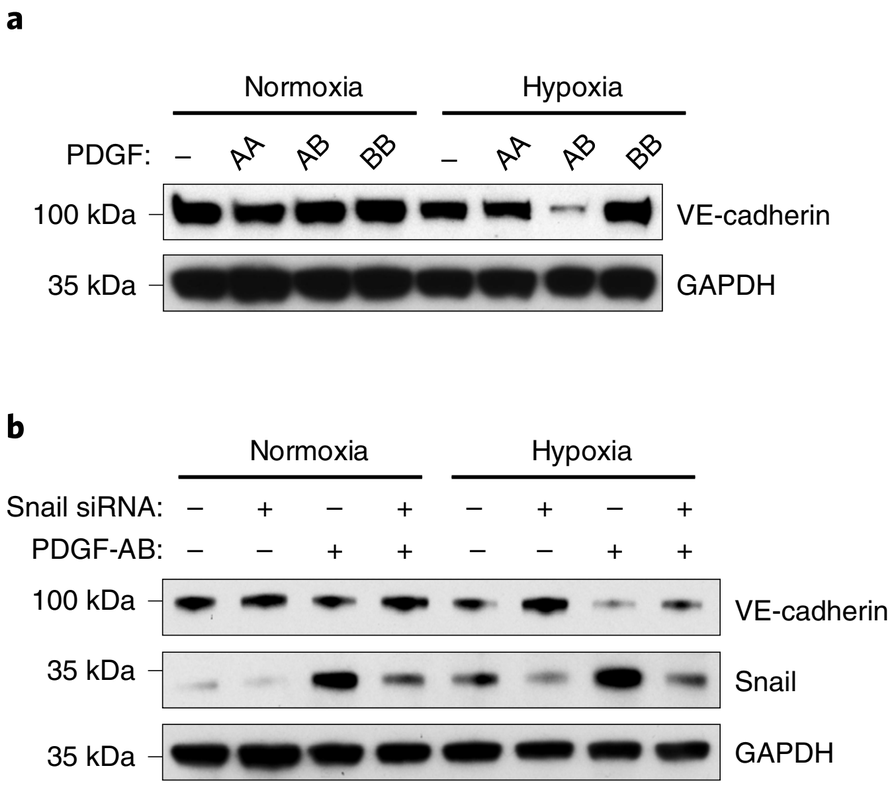

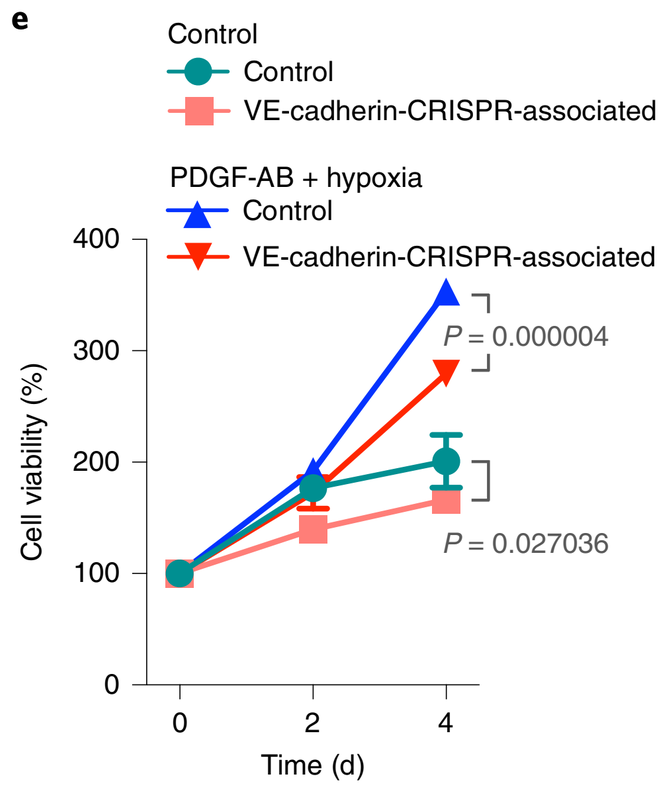

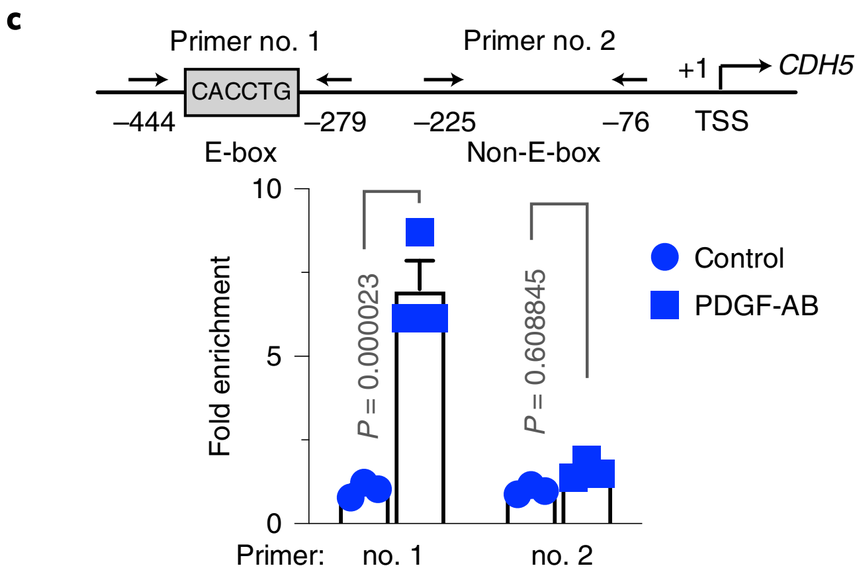

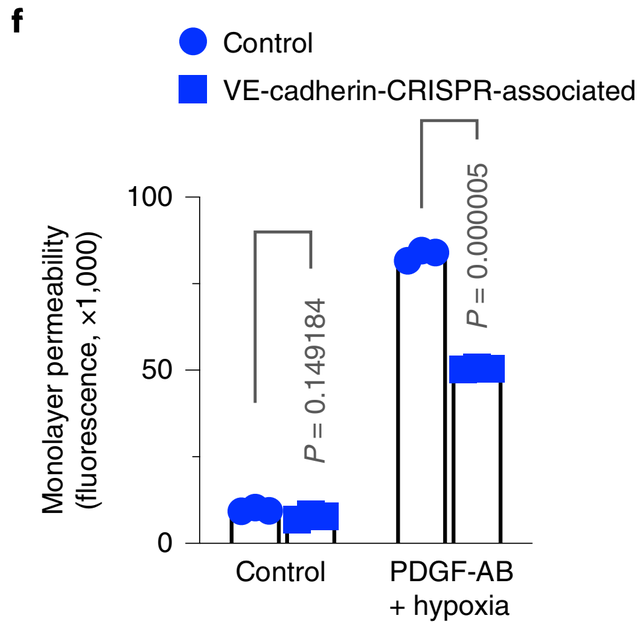

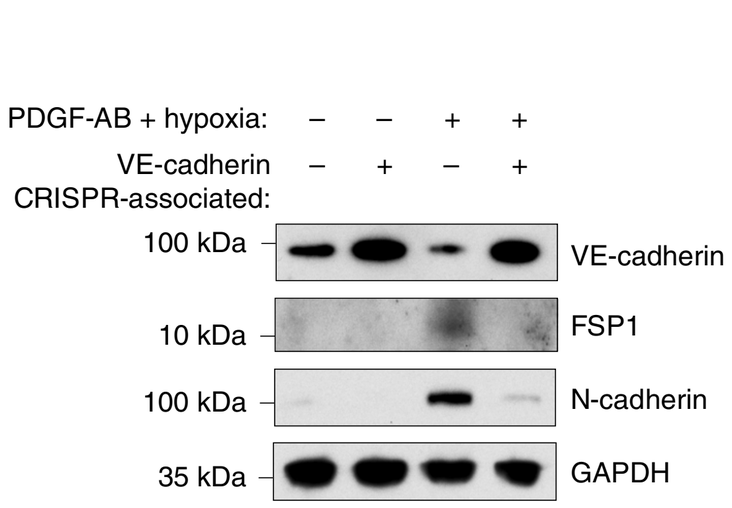

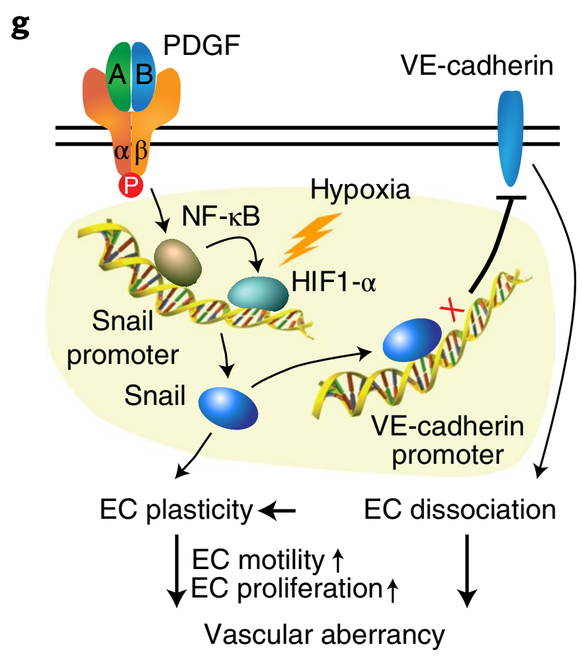

Fig. 5 | PDGF induces Snail binding to the VE-cadherin promoter, leading to VE-cadherin downregulated expression and mesenchymal phenotypes in ECs. a, Human cardiac microvascular ECs with 100 ng ml^{-1} PDGF-AA, PDGF-AB or PDGF-BB under normoxia or hypoxia. Cell lysates underwent immunoblotting. **b**, Human ECs were transfected with siRNA targeting Snail or the control scrambled sequence, followed by treatment with PDGF-AB. Cell lysates underwent immunoblotting. **a**,**b**, These experiments were repeated independently twice with similar results. **c**, Human ECs were treated with or without PDGF-AB under hypoxia, followed by ChIP analysis with anti-Snail antibody ($n = 3$ EC samples, mean ± s.e.m.). Statistical analysis by two-way ANOVA. **d**–**f**, Human ECs were transduced to express active CRISPR/sgRNA targeting VE-cadherin or the control sequence, followed by treatment with PDGF-AB under hypoxia. **d**, Cell lysate underwent immunoblotting. This experiment was repeated independently twice with similar results. **e**,**f**, Cells underwent proliferation ($n = 3$ EC samples, mean ± s.e.m.) (**e**) and permeability ($n = 3$ EC samples, mean ± s.e.m., 20 h after loading fluorescence dye) (**f**) analyses. Statistical analysis by two-way ANOVA. **g**, Schematic model. Under an MI condition, PDGF induces NF-κB-dependent Snail expression in ECs, which is further enhanced by hypoxia via HIF1-α. Snail induces EC plasticity by mesenchymal transcriptional activation. In addition, Snail binds to the VE-cadherin promoter, suppressing VE-cadherin transcription, facilitating EC plasticity that stimulates EC proliferation and migration, leading to vessel abnormalities.

PDGFR-β knockout and functional inhibition were verified by immunoblot analysis of isolated ECs and whole-heart tissues (Fig. 6b and Extended Data Fig. 5a). Interestingly, *Pdgfrb* deletion in ECs did not apparently affect basal angiogenesis in normal hearts (Extended Data Fig. 5b) or normal heart function (Fig. 6c,d), suggesting a dispensable role of endothelial PDGFR-β in physiological angiogenesis and normal tissue functions[23].

We next challenged these mice with MI surgery. Cardiac function was determined by long-axis echocardiogram. Notably, EC-specific PDGFR-β knockout improved cardiac function recovery after MI,

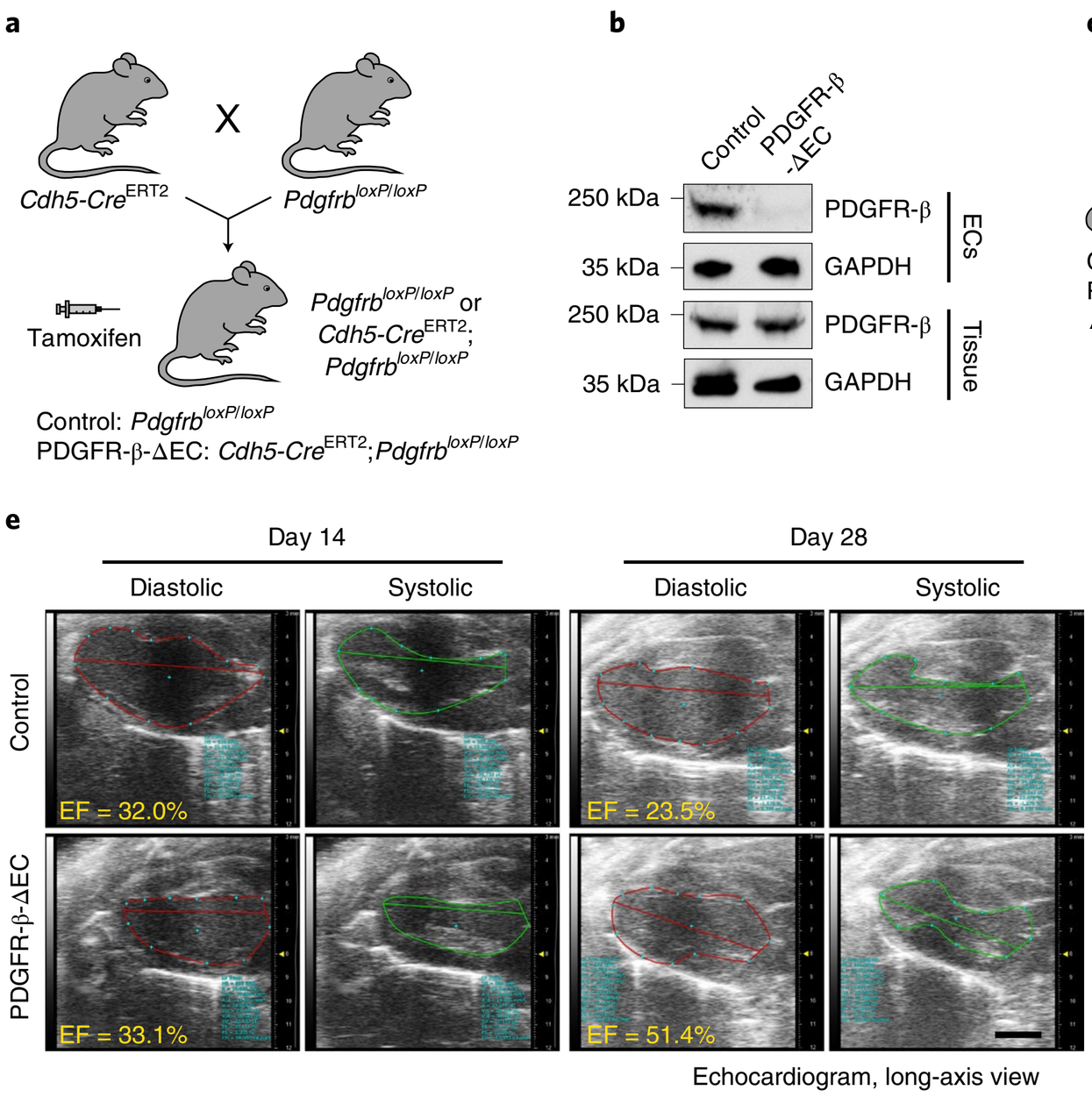
a
Cdh5-Cre^ERT2
X
Pdgfrb^loxP/loxP
Tamoxifen
Pdgfrb^loxP/loxP or Cdh5-Cre^ERT2; Pdgfrb^loxP/loxP
Control: Pdgfrb^loxP/loxP
PDGFR-β-ΔEC: Cdh5-Cre^ERT2;Pdgfrb^loxP/loxP
b
Control
PDGFR-β -ΔEC
250 kDa
PDGFR-β
35 kDa
GAPDH
ECs
250 kDa
PDGFR-β
35 kDa
GAPDH
Tissue
c
Ligation of LAD coronary artery
Control or PDGFR-β-ΔEC mice
0 3 14 28 (d)
Echocardiogram
Tissue collection and pathological analysis
d
EF (%)
80
60
40
20
0
P = 0.3304
Before MI
Control
PDGFR-β -ΔEC
e
Day 14
Day 28
Diastolic
Systolic
Diastolic
Systolic
Control
PDGFR-β-ΔEC
EF = 32.0%
EF = 23.5%
EF = 33.1%
EF = 51.4%
Echocardiogram, long-axis view
f
14 d after MI
28 d after MI
EF (%)
60
40
20
Control
PDGFR-β -ΔEC
EF change (%)
60
40
20
0
–20
P = 0.0004
Control
PDGFR-β -ΔEC
g
14 d after MI
28 d after MI
SV (μl)
50
25
0
Control
PDGFR-β -ΔEC
SV change (%)
100
50
0
–50
P = 0.0137
Control
PDGFR-β -ΔEC
h
14 d after MI
56 d after MI
EF (%)
50
40
30
20
Control
PDGFR-β -ΔEC
EF change (%)
20
0
–20
–40
P = 0.0005
Control
PDGFR-β -ΔEC
i
Infarction size (%)
80
40
0
P = 0.0270
Control
PDGFR-β -ΔEC
j
Control
PDGFR-β-ΔEC
y
z
x
Confocal imaging, 3D reconvolution; CD31
Vessel area (%)
20
10
0
P = 0.0128
Length (a.u.)
8
4
0
P = 0.0090
Junction (a.u.)
15
10
5
0
P = 0.0245
End point (a.u.)
8
4
0
P = 0.0804
Lacunarity (a.u.)
1.0
0.5
0
P = 0.0009
Control
PDGFR-β -ΔEC
k
Control
PDGFR-β-ΔEC
y
z
x
Light sheet imaging; DyLight 649-conjugated lectin
Lectin perfusion in MI (fluorescence, ×10^7)
15
10
5
0
P = 0.0005
Control
PDGFR-β -ΔEC

Fig. 6 | PDGFR-β deletion in ECs normalizes the vasculature and improves cardiac function recovery after MI. a, Breeding strategy for the generation of control and PDGFR-β-ΔEC mice. **b**, Aortic ECs were isolated. Lysates from ECs and the cardiac tissue lysate underwent immunoblotting. This experiment was repeated independently twice with similar results. **c**–**k**, MI was induced in control and PDGFR-β-ΔEC mice. **c**, Schematic approach. **d**–**h**, Mice were analyzed by echocardiography. EF was measured before MI (mean ± s.e.m., $n = 6$ mice for the control group and $n = 4$ mice for the PDGFR-β-ΔEC group) (**d**), at days 14 and 28 (**e**–**g**) or at days 14 and 56 after MI (**h**). **e**, Representative echocardiogram images. Scale bar, 2 mm. **f**,**g**, Left: EF (**f**) and SV (**g**) values in individual mice. Right: Percentage of EF (**f**) and SV (**g**) changes from days 14 to 28 (mean ± s.e.m., $n = 8$ mice for the control group and $n = 9$ mice for the PDGFR-β-ΔEC group). Statistical analysis by two-tailed Student's *t*-test. **h**, Left: EF values in individual mice. Right: Percentage of EF changes from days 14 to 56 (mean ± s.e.m., $n = 6$ mice for the control group and $n = 5$ mice for the PDGFR-β-ΔEC group). Statistical analysis by two-tailed Student's *t*-test. **i**, Cardiac tissues were collected at day 28 and infarction size was analyzed (mean ± s.e.m., $n = 8$ mice). Statistical analysis by two-tailed Student's *t*-test. **j**, Twenty-one days after MI, MI tissue was collected and immunostained with anti-CD31 antibody, followed by 3D confocal scanning. Left: Representative images in the infarct zone. 3D scale bar, 50 μm. Right: Quantified results (mean ± s.e.m., $n = 3$ mice for the control group and n = 4 mice for the PDGFR-β-ΔEC group). Statistical analysis by two-tailed Student's *t*-test. **k**, Twenty-eight days after MI, mice were perfused with DyLight 649-conjugated lectin and cardiac tissues were analyzed by light sheet fluorescence imaging. Left: Representative images. 3D scale bar, 1mm. Right: Quantitative results (mean ± s.e.m., $n = 7$ mice for the control group and $n = 6$ mice for the PDGFR-β-ΔEC group). Statistical analysis by two-tailed Student's *t*-test.

as evidenced by a 28.8% increase in ejection fraction (EF) from day 14 to day 28 after MI in PDGFR-β knockout mice, in contrast to a slight EF decrease (−9.0%) during the same period in control mice (Fig. 6e,f). Similarly, stroke volume (SV) was increased by 38.3% in PDGFR-β knockout mice, compared to a −9.6% decrease in control mice (Fig. 6g). The echocardiogram showed that PDGFR-β knockout enhanced myocardial contractility in the infarct border zone (Extended Data Movie 1). The beneficial effects of PDGFR-β knockout on cardiac functions were sustained to eight weeks after MI (Fig. 6h). Moreover, PDGFR-β knockout reduced infarction size in the hearts (Fig. 6i). Importantly, three-dimensional (3D) confocal imaging analysis showed that PDGFR-β deletion in ECs attenuated vessel abnormalities in the MI tissues, as indicated by apparently normalized vasculature, reduced vessel area, length and junction, and increased lacunarity (Fig. 6j). Likewise, PDGFR-β knockout promoted cardiac perfusion (Fig. 6k). In addition, PDGFR-β deletion in ECs did not affect vascular density in the border zone (Extended Data Fig. 6). Consistent with these findings, immunofluorescence studies showed that PDGFR-β deletion moderately attenuated the densities of total vessels and Ki-67$^+$ proliferative ECs in MI tissues (Extended Data Fig. 7a–c). Moreover, genetic ablation of PDGFR-β reduced Snail and FSP1 expression in MI-associated ECs (Extended Data Fig. 7d,e).

PDGFR-β knockout in ECs improves cardiac repair after MI. Furthermore, PDGFR-β knockout in ECs promoted cardiac perfusion improved cardiac repair after MI, as indicated by smaller infarct size (Fig. 6i), better organized structure and increased cardiomyocyte survival in the infarct zone (Fig. 7a,b). Interestingly, these survived cardiomyocytes were associated with normalized vasculature in the MI tissue of PDGFR-β knockout mice but not with aberrant vasculature in the MI tissue of control mice (Fig. 7c). Our single-nucleus RNA-seq analysis of MI-associated tissues confirmed that PDGFR-β deletion reduced Snail expression in ECs in a time-dependent manner (Extended Data Fig. 8) and showed that genetic ablation of PDGFR-β stimulated cardiomyocyte expression of proliferation-associated genes including *Ccna2*, *Pcna*, *Top2a* and *Mcm6*, particularly at day 14 after MI (Fig. 7d,e), suggesting time-dependent positive effects on cardiomyocyte proliferation. Furthermore, PDGFR-β knockout in ECs inhibited the expression of pro-apoptotic *Bax* but promotes the expression of antiapoptotic *Bcl2* in cardiomyocytes at day 14 after MI (Fig. 7f), suggesting time-dependent antiapoptotic effects on myocytes. Immunofluorescence analysis verified enhanced numbers of proliferating cell nuclear antigen (PCNA)$^+$ cardiomyocytes in PDGFR-β knockout mice (Fig. 7g) and reduced cardiomyocyte apoptosis in the infarct heart (Fig. 7h). In addition, PDGFR-β knockout in ECs also temporally stimulated cardiomyocyte metabolism, as evidenced by time-dependent increases in the expression of metabolism-associated genes (Extended Data Fig. 9). These findings collectively suggest that PDGF-mediated endothelial plasticity drives vessel abnormalities, leading to impeded cardiac repair and function recovery after MI.

PDGFR inhibition enhances cardiac function recovery after MI. To test PDGFR as a target for vessel normalization therapy, MI was induced in mice, followed by administration with saline or the pharmacological PDGFR inhibitor crenolanib (Fig. 8a). Considering a role of PDGF for pericyte coverage during the late phase of neovascularization, treatment was daily rendered during the first three weeks after MI to avoid disrupting vascular maturation in the later phase. Notably, crenolanib enhanced cardiac function recovery at day 21 after MI, as evidenced by an EF increase (by +14.5%) in crenolanib-treated mice, compared with an EF decrease (by −16.7%) in saline-treated mice during that period (Fig. 8b and Extended Data Fig. 10a). Moreover, MI induced left ventricular wall motion abnormalities, as indicated by weak wall motion at day 7 after MI; crenolanib, but not saline, partially restored the anterior wall motion at day 21 after MI (Extended Data Fig. 10b). Consistent with the improved cardiac function recovery after MI, crenolanib enhanced cardiac repair after MI (Extended Data Fig. 10c,d) but did not affect vascular density in the infarct and border zones (Extended Data Fig. 10e).

Fig. 7 | Endothelial-specific deletion of PDGFR-β promotes tissue repair and cardiomyocyte function after MI. MI was induced in control and PDGFR-β-ΔEC mice. **a**,**b**, Twenty-one days after MI induction, cardiac tissues were collected. Sections were stained with Masson's trichrome stain. **a**, Representative images. Scale bar, 500 μm. The arrows indicate the epicardium. **b**, Quantified cardiomyocyte area (mean ± s.e.m., $n = 5$ mice). Statistical analysis by unpaired two-tailed Student's *t*-test. **c**, Seven days after MI, MI tissue was collected. Tissue sections were immunostained with anti-CD31 and anti-tropomyosin antibodies. Representative immunofluorescence images in the infarct zone are shown ($n = 3$ mice). Scale bar, 100 μm. **d**–**f**, Fourteen and 28 d after MI, MI tissue was collected and analyzed by single-nucleus RNA-seq. **d**, UMAP analysis of the transcriptome gene signature. **e**,**f**, Expression of proliferation- (**e**) and apoptosis-associated (**f**) genes in cardiomyocytes. **g**,**h**, Fourteen days after MI induction, cardiac tissues were collected. **g**, Sections were stained with anti-tropomyosin and anti-PCNA antibodies. Left: Representative images in the infarct zone. Scale bar, 100 μm. The arrows indicate PCNA$^+$ cardiomyocytes. Right: Quantified results (mean ± s.e.m., $n = 6$ mice). Statistical analysis by two-tailed Student's *t*-test. **h**, Sections were stained with anti-tropomyosin antibody and TUNEL. Left: Representative images in the infarct zone. Scale bar, 100 μm. The arrows indicate apoptotic TUNEL$^+$ cardiomyocytes. Right: Quantified results (mean ± s.e.m., $n = 6$ mice). Statistical analysis by two-tailed Student's *t*-test.

We finally tested experimental therapy with a polymer–lipid nanoparticle-based system for targeted delivery of PDGFR-β siRNA into ECs (Fig. 8c,d)[24,25], which is not expected to disrupt PDGF-mediated pericyte function and vessel maturation. Treatment of MI-bearing mice with nanoparticles containing PDGFR-β siRNA (siPDGFR-β nanoparticles) showed similar therapeutic efficacy, compared with crenolanib (Fig. 8e). siPDGFR-β nanoparticles markedly improved vessel function, as indicated by an about

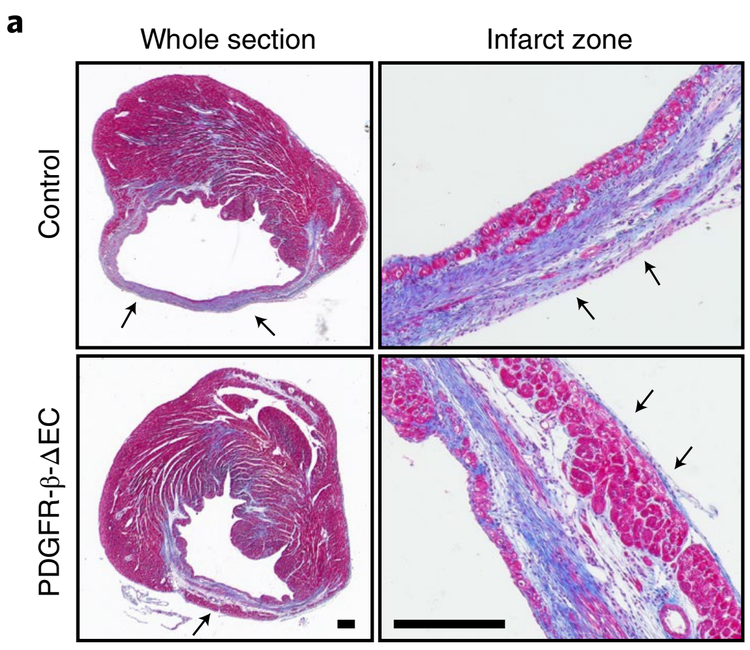

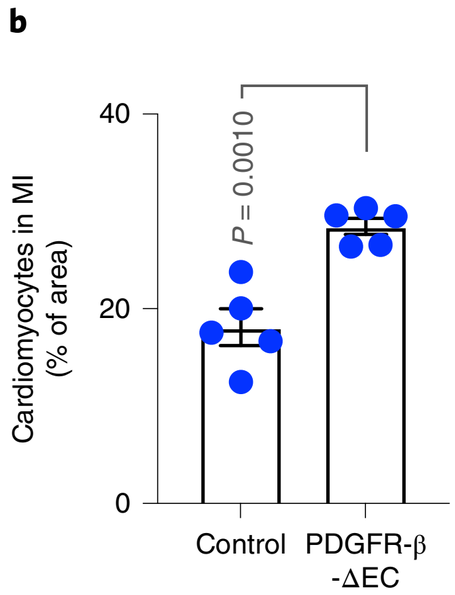

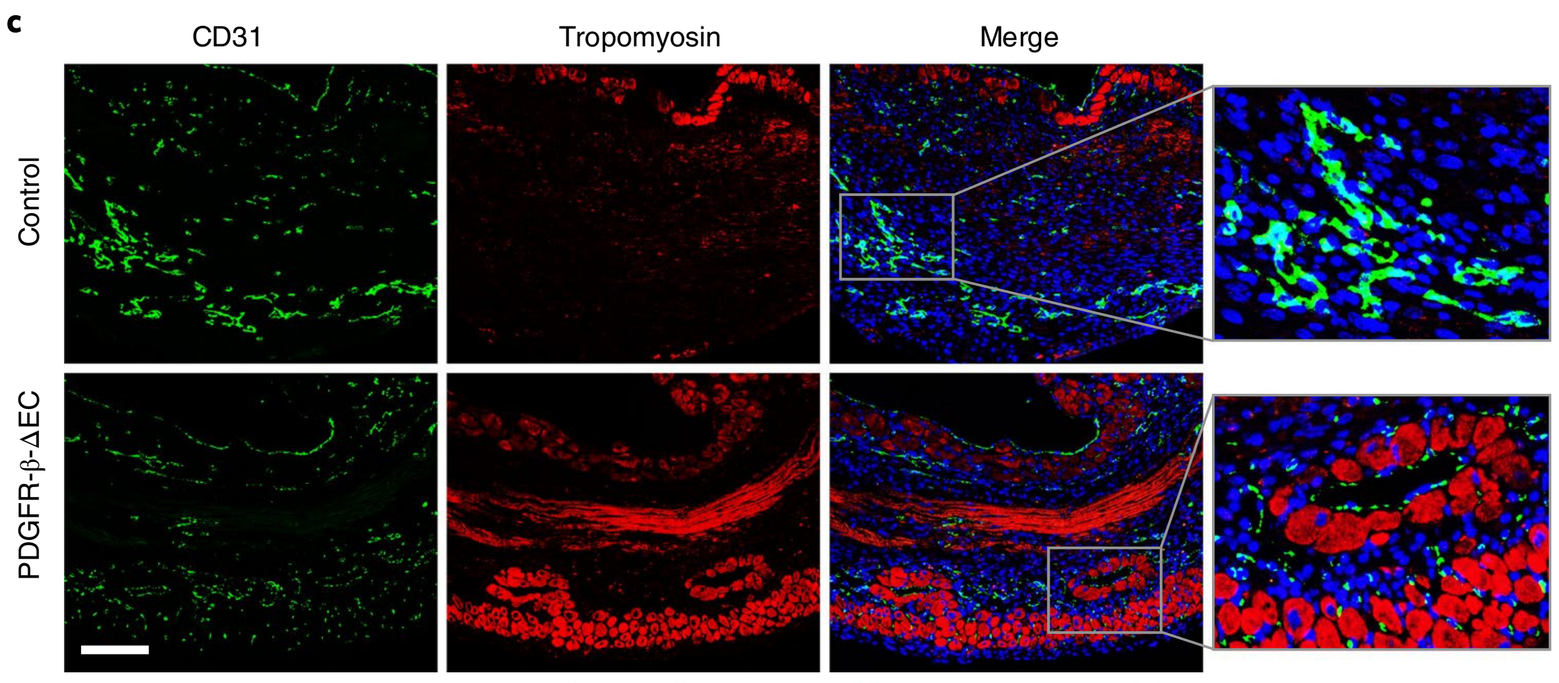

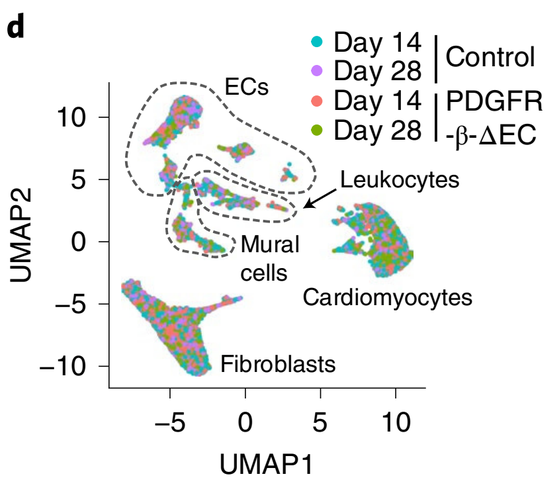

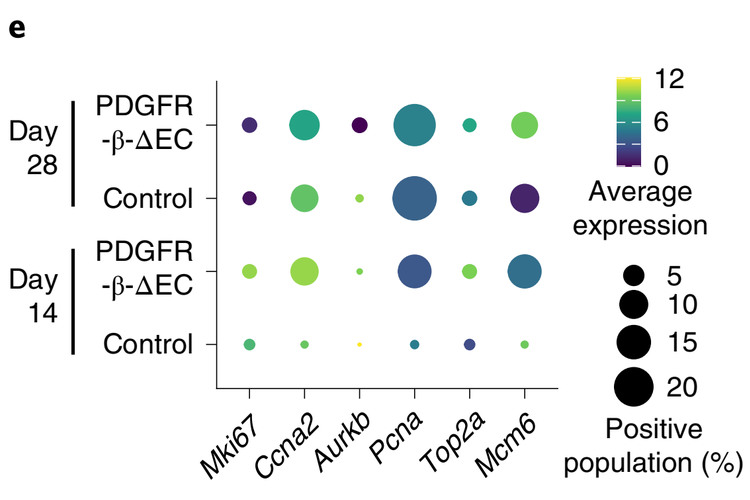

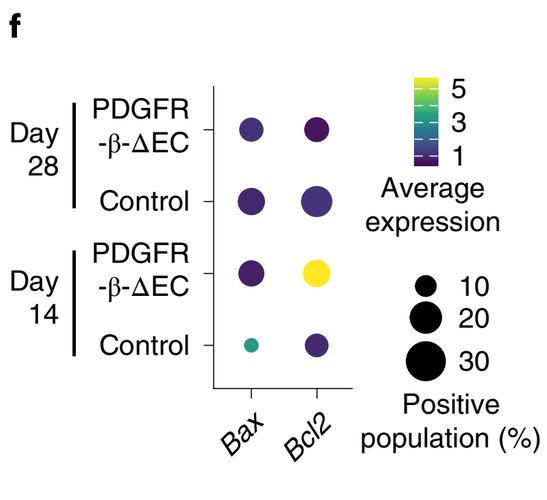

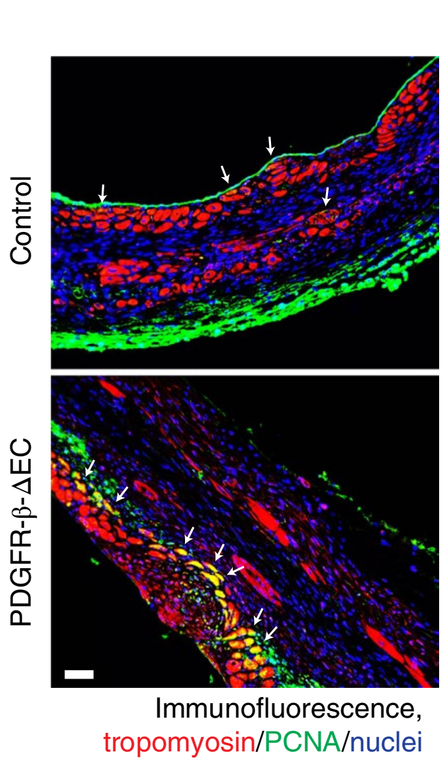

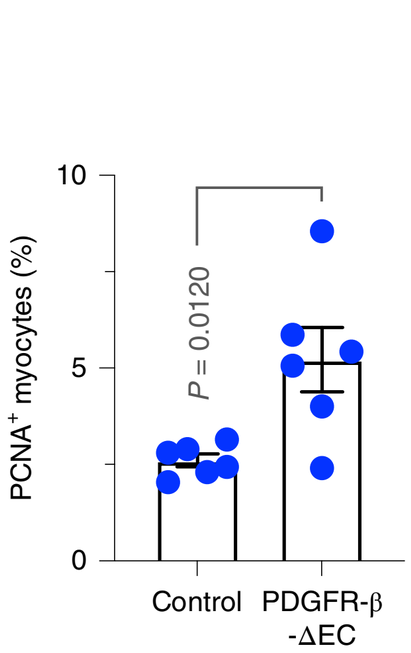

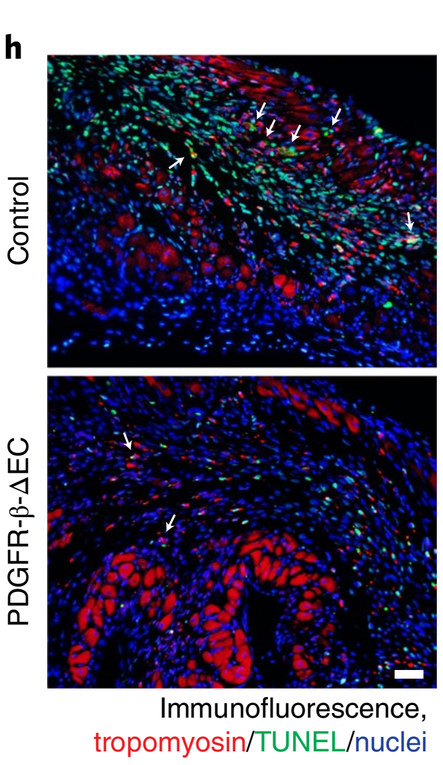

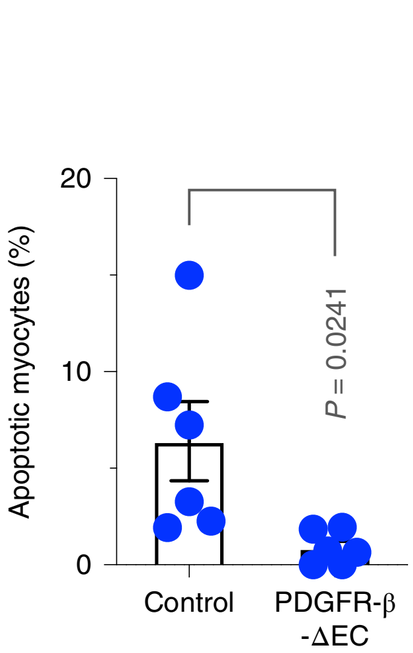

twofold increase in MI tissue perfusion detected by single-photon emission computerized tomography (SPECT) (Fig. 8f) and by an approximate 30% decrease in the nonperfused volume of MI tissues detected by lectin perfusion (Fig. 8g). Collectively, these data show that PDGFR inhibition or targeted PDGFR-β ablation in ECs improves tissue perfusion and repair and promotes cardiac function recovery after MI.

In addition, we tested endothelial plasticity in infarcted or healthy cardiac tissue from humans. Immunofluorescence analysis of the tissue sections showed Snail expression in MI-associated von Willebrand factor (vWF)$^+$ ECs, particularly in scar-containing MI tissues (Fig. 8h), suggesting robust endothelial–mesenchymal transition in MI-associated human ECs in accordance with our results with mouse studies.

Discussion

Neovascularization is crucial for tissue repair after ischemia. As such, pro-angiogenic therapy that targets VEGF, placental growth factor and basic fibroblast growth factor to promote neovascularization in ischemic tissue has been extensively exploited in the clinic by gene-, protein- and cell-based treatments; however, therapeutic efficacy is limited[2–6]. Likewise, ischemia itself induces angiogenesis through HIF1-α-dependent expression of VEGF[26–28] but fails to efficiently generate reperfusion and improve cardiac function recovery. Conceptually, angiogenic factors, such as VEGF, stimulate EC migration and proliferation to enhance sprouting angiogenesis; however, they could also induce vessel abnormalities and instability, for example, vascular leakiness and dilation[29,30]. Based on these findings and our results, we suggest that the difficulties and failures of pro-angiogenic therapy could be explained by nonproductive neovascularization, that is, induced angiogenesis, albeit robust, is defective due to structural and functional abnormalities in the newly formed vasculature. Our work defines MI-associated aberrant vascularity and suggests that vessel normalization may join therapeutic angiogenesis as promising strategies for improving cardiac repair after MI.

We propose endothelial plasticity as a potential target for vessel normalization therapy in MI. Our recent studies indicate that tumor-associated ECs acquire mesenchymal phenotypes to enhance cell proliferation and migration, thereby promoting vessel sprouting and outgrowth and inducing vascular abnormalities in glioma; these cells retain their EC functions in the cancer microenvironment[16]. Probably due to a similar hypoxic, inflammatory microenvironment in the infarcted cardiac tissue, MI-associated ECs undergo endothelial–mesenchymal transition to generate aberrant vasculature that cannot not efficiently deliver oxygen, nutrients and possibly circulating stem cells to fuel cardiac repair after MI. Our work suggests that acquisition of genetic reprogramming to express a mesenchymal gene signature in ECs enhances their ability to proliferate, migrate and dissociate, thereby leading to nonproductive angiogenesis, possibly affecting most of fast-growing MI-associated capillaries, which serves as a target for vessel normalization therapy in MI. Considering a dispensable role of PDGFR-β-mediated endothelial plasticity for developmental angiogenesis[23], targeting endothelial–mesenchymal transition may represent a safe, selective strategy for vessel normalization therapy.

Previous work suggested that endothelial–mesenchymal transition contributes to de novo fibroblast generation during cardiac fibrosis[11]. However, our single-cell transcriptome study shows that ECs keep their endothelial identity but acquire mesenchymal and proliferative gene signatures three weeks after MI, serving as evidence for partial endothelial–mesenchymal transition and suggesting that a major function of endothelial plasticity is to enhance EC mitosis and motility and induce vessel abnormalities during this period. Notably, we showed that inhibition of endothelial–mesenchymal transition by PDGFR-β knockout in ECs does not affect collagen deposition after MI, indicating that endothelial–mesenchymal transition does not contribute to fibroblast generation in this time frame. Consistent with our findings, a previous study using laser capture microdissection showed that Cdh5-Cre-traced ECs express endothelial–mesenchymal transition-associated genes after MI, suggesting that partial endothelial–mesenchymal transition may be associated with EC clonal expansion and ischemia-induced vessel growth[13]. Interestingly, a recent report showed slight increases in expression of endothelial–mesenchymal transition markers in Pdgfb-Cre-traced, MI-associated ECs one week after MI; however, no EC subpopulations with switched lineage were detectable in the infarct tissue[14], suggesting that endothelial–mesenchymal transition is a dynamic process subject to temporal regulation. Consistent with a more recently published elegant work showing a transient mesenchymal activation in cardiac ECs after MI[15], our study shows robust mesenchymal gene expression after MI, which reaches a peak one week after MI, followed by a gradual decrease to a lower level for three weeks, contributing to EC dysfunction and vessel abnormalities. We suggest that the retained mesenchymal activation, albeit in small proportion of ECs (5–20%; Fig. 1i), could disrupt vessel integrity since the teamwork of entire ECs is required for vascular homeostasis.

The regulatory mechanisms underlying endothelial–mesenchymal transition are largely unclear. Endothelial plasticity could be mediated through FGF, transforming growth factor (TGF)-β, bone morphogenetic protein, HGF/c-Met and Notch pathways[12,16,31–33]. Consistent with this work, we previously identified a Snail-mediated mechanism controlling endothelial–mesenchymal transition in brain ECs under cancer conditions; namely, PDGF induced NF-κB-dependent Snail expression, leading to VEGFR-2 downregulation and EC resistance to anti-VEGF treatment[23]. Our study reveals that ischemia or hypoxia serves as a trigger to amplify NF-κB-mediated Snail expression through an NF-κB–HIF-1a–Snail mechanism, driving robust Snail expression and sequent endothelial–mesenchymal transition and aberrant vascularization after MI. Snail plays a

Fig. 8 | Pharmacological inhibition or nanoparticle-mediated targeting of PDGFR improves cardiac function recovery after MI. a,**b**, MI was induced in mice, followed by administration with saline or 15 mg kg^{-1} crenolanib. **a**, Schematic approach. **b**, Cardiac function was analyzed by long-axis echocardiogram ($n=11$ mice). Left: EF values in individual mice. Right: Percentage of EF changes from days 7 to 21 (mean ± s.e.m.). Statistical analysis by two-tailed Student's *t*-test. **c**, Mouse cardiac microvascular ECs were pretreated with mouse CCM and treated with siControl or siPDGFR-β nanoparticles, followed by immunoblot analysis. This experiment was repeated independently twice with similar results. **d**,**e**, MI was induced in mice, followed by the administration of siRNA nanoparticles. **d**, Schematic approach. **e**, Cardiac function was analyzed by long-axis echocardiogram ($n=9$ mice for the siControl nanoparticle group and $n=7$ mice for the siPDGFR-β nanoparticle group). Left: EF values in individual mice. Right: Percentage of EF changes from days 7 to 28 (mean ± s.e.m.). Statistical analysis by two-tailed Student's *t*-test. **f**, Mice underwent cardiac SPECT scanning. Left: Representative images. Scale bar, 1 mm. Right: Quantified results of perfusion rate in the MI region (mean ± s.e.m., $n=5$ mice). Statistical analysis by two-tailed Student's *t*-test. **g**, Mice were perfused with DyLight 649-conjugated lectin 28 d after MI induction and underwent light sheet fluorescence imaging. Left: Representative images. 3D scale bar, 0.5 mm. Right: Quantified results of unperfusion volume in cardiac tissues (mean ± s.e.m., $n=4$ mice). Statistical analysis by unpaired two-tailed Student's *t*-test. **h**, Human heart sections from healthy controls ($n=5$ humans) or cardiac patients with pathological diagnosis of acute MI ($n=14$ patients), granulation tissue ($n=10$ patients) and scar-containing tissue ($n=7$ patients) were immunostained with anti-vWF and anti-Snail antibodies. Snail-expressing ECs in vWF$^+$ ECs were counted and quantified (mean ± s.e.m.). Statistical analysis by two-tailed Student's *t*-test.

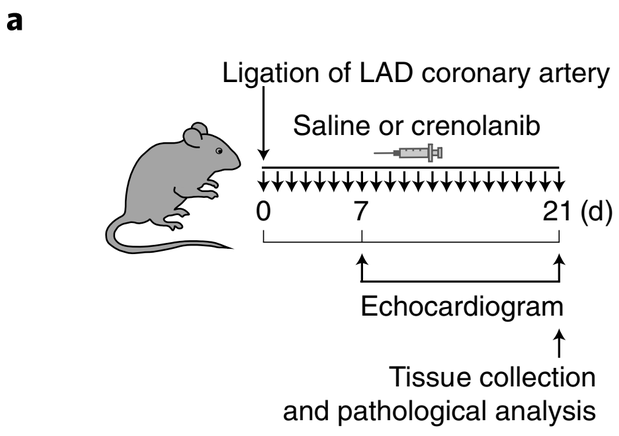
a
Ligation of LAD coronary artery
Saline or crenolanib
0
7
21 (d)
Echocardiogram
Tissue collection
and pathological analysis

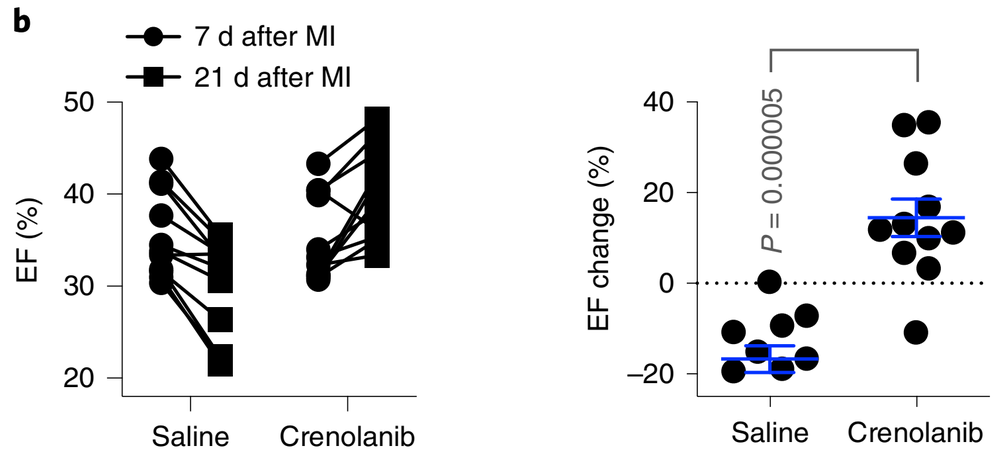
b
7 d after MI
21 d after MI
EF (%)
50
40
30
20
Saline
Crenolanib
EF change (%)
40
20
0
–20
P = 0.000005
Saline
Crenolanib

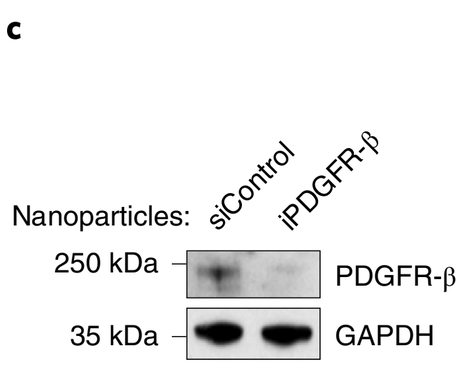
c
Nanoparticles:
siControl
iPDGFR-β
250 kDa
PDGFR-β
35 kDa
GAPDH

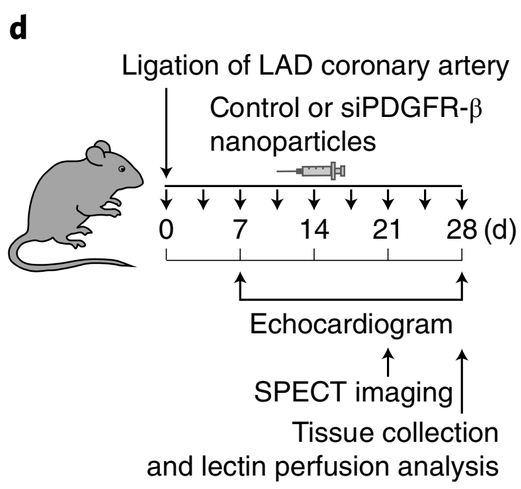
d
Ligation of LAD coronary artery
Control or siPDGFR-β
nanoparticles
0
7
14
21
28 (d)
Echocardiogram
SPECT imaging
Tissue collection
and lectin perfusion analysis

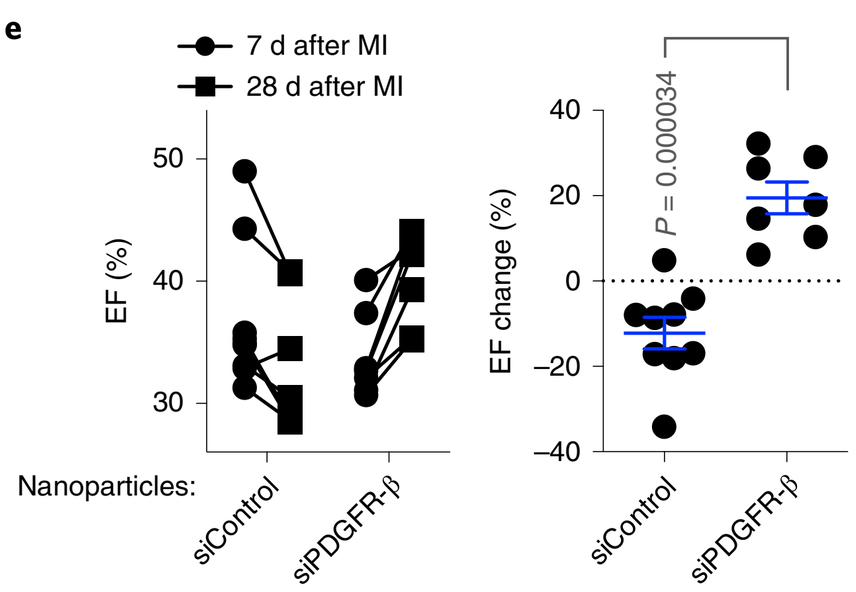
e
7 d after MI
28 d after MI
EF (%)
50
40
30
Nanoparticles:
siControl
siPDGFR-β
EF change (%)
40
20
0
–20
–40
P = 0.000034
siControl
siPDGFR-β

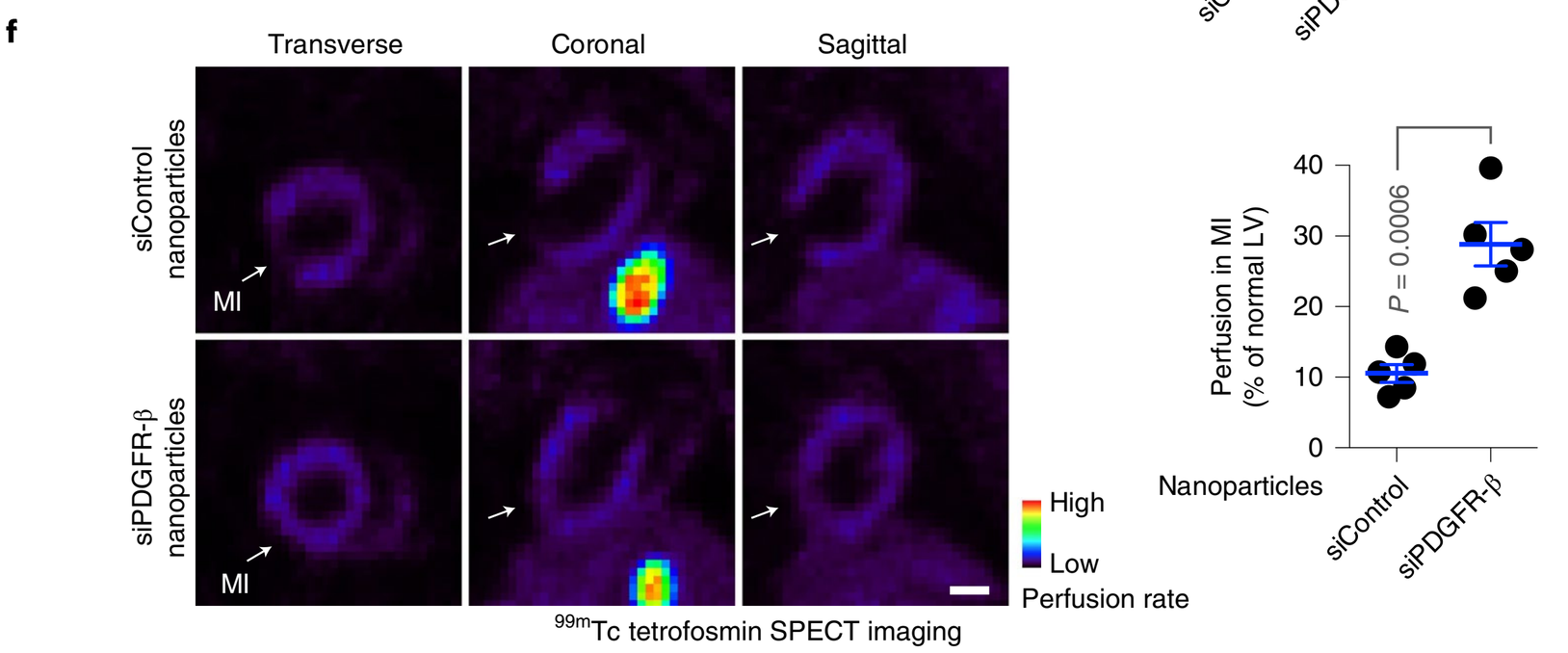
f
Transverse
Coronal
Sagittal
siControl nanoparticles
siPDGFR-β nanoparticles
MI
MI
High
Low
Perfusion rate
99mTc tetrofosmin SPECT imaging
Perfusion in MI
(% of normal LV)
40
30
20
10
0
P = 0.0006
Nanoparticles
siControl
siPDGFR-β

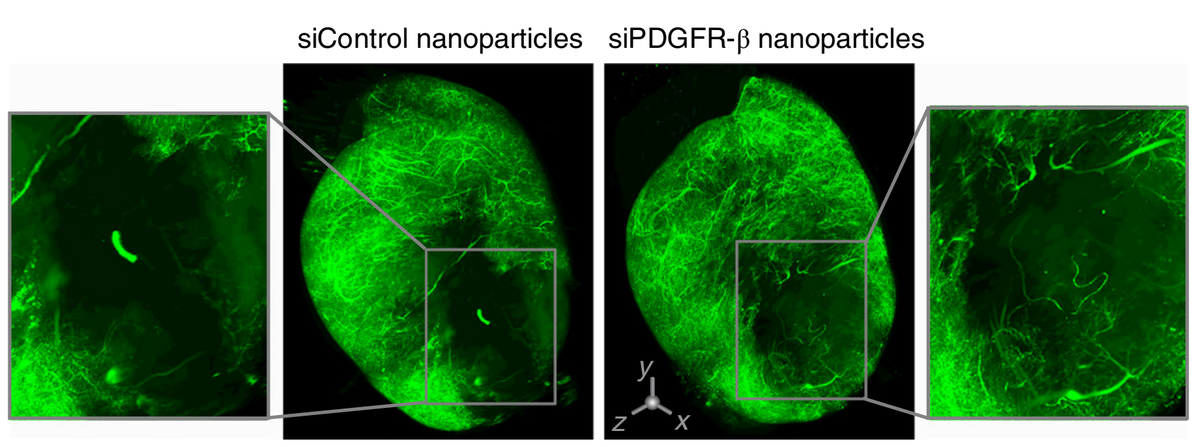
g
siControl nanoparticles
siPDGFR-β nanoparticles
y
z
x
Light sheet fluorescence imaging, DyLight 649-conjugated lectin
Unperfused
volume (mm3)
15
10
5
0
P = 0.0387
Nanoparticles
siControl
siPDGFR-β

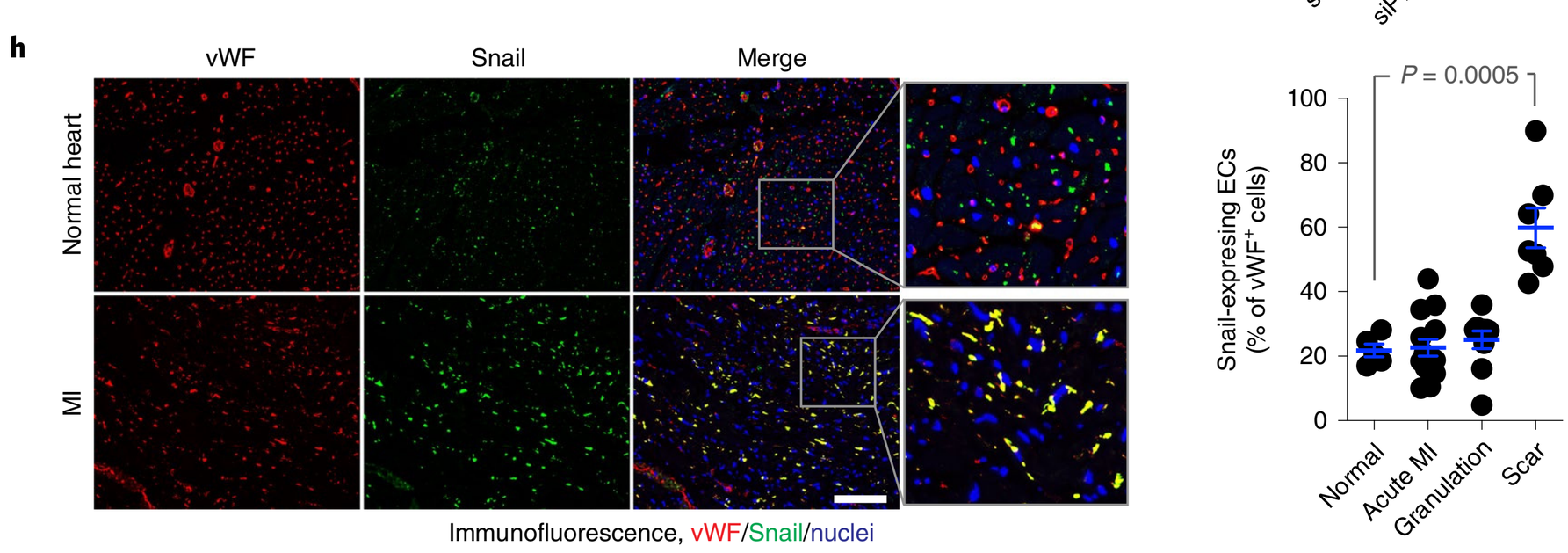
h
vWF
Snail
Merge
Normal heart
MI
Immunofluorescence, vWF/Snail/nuclei
Snail-expresing ECs
(% of vWF+ cells)
100
80
60
40
20
0
P = 0.0005
Normal
Acute MI
Granulation
Scar

key role for epithelial–mesenchymal transition in tumor cells[21,34]; it binds to the promoter region of cadherins, suppressing their transcription and facilitating epithelial–mesenchymal transition in ECs[35,36]. Supportive of our work, NF-κB and HIF1-α contribute to the regulation of Snail expression during epithelial–mesenchymal transition[37–40]. Regarding endothelial–mesenchymal transition, recent studies suggested that Snail is critical for endothelial plasticity induced by hypoxia, TGF-β treatment or shear stress[41–43]. Consistent with our work, previous studies suggested that Snail acts as a transcriptional suppressor of VE-cadherin in trophoblast cells or ECs under cancer conditions[44,45]. Our work shows that VE-cadherin downregulation induces endothelial–mesenchymal transition, suggesting that a critical role for destabilization of VE-cadherin-mediated adherens junctions has a role in endothelial plasticity regulation.

PDGF has a multifaceted role in cardiac repair after MI, acting mainly through spatiotemporal regulation of angiogenesis and fibrosis. PDGFs, particularly PDGF-BB, stimulate EC proliferation and enhance vessel functionality with maturation by promoting pericyte recruitment to the newly formed vessels[46–48]. Our work suggests that excessive PDGF-AB, possibly derived from hypoxic cardiomyocytes and fibroblasts, induces endothelial–mesenchymal transition-mediated vessel abnormalities in an ischemic microenvironment. As such, we showed that PDGF inhibition normalizes the vasculature and improves cardiac function recovery after MI. Consistent with our findings, previous work showed that imatinib, a pharmacological inhibitor of PDGFR, ABL and c-Kit, does not affect vascular density but moderately improves cardiac function after MI in rats[49]. Moreover, antibody-based PDGFR-β blockade does not reduce capillary density in the injured tissue after transient ischemia followed by reperfusion, but it impedes vascular maturation probably due to impaired pericyte coverage[50], suggesting that MI therapy by PDGF inhibition requires temporal optimization to avoid disturbing vessel maturation in the later phase of cardiac repair. In addition, considering the role of PDGFs as mitogens for fibroblasts, PDGFR inhibition may inhibit cardiac interstitial fibrosis to improve ventricular dysfunction[49]. Notably, our work shows that PDGFR-β knockout in ECs robustly improves cardiac repair and functional recovery after MI, suggesting a major beneficial effect of PDGF inhibition via vessel normalization.

In summary, we characterized MI-associated vascular aberrancy, which is driven by endothelial plasticity. We identified a PDGF–NF-κB–HIF1-α–Snail axis that induces VE-cadherin downexpression, mesenchymal-like transcriptional activation and vessel abnormalities. Notably, genetic ablation or targeted disruption of PDGF signaling normalizes the vasculature and improves cardiac function recovery after MI. As such, vessel normalization by targeting PDGF/Snail-mediated endothelial plasticity may offer exciting opportunities to treat ischemic heart disease.

Methods

Mice. *Cdh5-Cre*^{ERT2};*Rosa-LSL-tdTomato* and *Tie2-Cre*;*Rosa-LSL-tdTomato* mice were generated by crossing *Rosa-LSL-tdTomato* mice (The Jackson Laboratory) with *Tie2-Cre* mice (The Jackson Laboratory) and *Cdh5-Cre*^{ERT2} mice (generated by R. Adams, Max Planck)[51]. *Cdh5-Cre*^{ERT2}; *Pdgfrb*$^{loxP/loxP}$ mice were generated by crossing *Pdgfrb*$^{loxP/loxP}$ mice (The Jackson Laboratory) with *Cdh5-Cre*^{ERT2} mice. For mice with a *Cdh5-Cre*^{ERT2} background, 2-week-old animals were injected intraperitoneally with 0.1 ml of 5 mg ml^{-1} tamoxifen daily for 5 consecutive days. All animals were housed at room temperature with a 12-h light–12-h dark cycle and fed a standard chow diet ad libitum with free access to water in the Association for the Assessment and Accreditation of Laboratory Animal Care-accredited animal facility of the University of Pennsylvania. All experiments with mice were performed in accordance with a protocol approved by the Institutional Animal Care and Use Committee at the University of Pennsylvania.

MI induction. MI was induced by ligation of the LAD coronary artery as we described previously[52]. Briefly, mice (half males and half females, 6–8 weeks old) were given buprenorphine sustained release (1 mg kg^{-1}) 1 h before surgery and then anesthetized by injection of 100 mg kg^{-1} ketamine and 10 mg kg^{-1} xylazine. Mice were intubated endotracheally and ventilated at 100 breaths per minute using a rodent ventilator (Kent Scientific). After sternotomy, the proximal LAD was ligated with 8-0 Prolene thread; the ligation was verified by blanching and dysfunction of the anterior wall. For the sham operation, the suture was passed around the coronary artery but not ligated. Mice were placed under isoflurane (1–3%) to maintain an adequate anesthesia during surgery.

Echocardiography. To evaluate LV function by echocardiography, as recommended by the American Society of Echocardiography[53], we performed LV volumetric measurements using a two-dimensional (2D) LV long-axis view with a Vevo 2100 imaging system (VisualSonics) and an ultra-high-frequency linear array transducer (MicroScan MS400 18–38 MHz transducer; VisualSonics). EF and SV were analyzed using the Vevo Lab v.3.2.0 software (VisualSonics). Echo imaging was performed on mice 7, 14, 21, 28 or 56 d after MI surgery. In some experiments, M-mode images were obtained to show the motion of the LV anterior wall. After LAD ligation, mice underwent echocardiography to monitor the consistence of infarction; mice with similar EF (30–50%) at day 3 (control versus PDGFR-β-Δ-EC mice) or 7 (for PDGFR inhibition) were chosen for further analyses.

scRNA-seq analysis. MI was induced in *Cdh5-Cre*^{ERT2};*Rosa-LSL-tdTomato* mice. Then, 0, 1, 2, 3 and 8 weeks after the MI surgery or sham operation, mice were euthanized and perfused with PBS supplemented with EDTA and hearts were collected. Infarcted tissue was dissected under a stereomicroscope and digested with DNase (1 mg ml^{-1}, catalog no. D4527; Sigma-Aldrich) in papain digestion medium (23.6 mg papain (APL; Worthington Biochem), 4.5 mg EDTA and 4.5 mg L-Cysteine (catalog no. C7352; Sigma-Aldrich) in 25 ml Earle's Balanced Salt Solution (catalog no. E2888; Sigma-Aldrich)). The single-cell suspension was prepared after filtering with a mesh strainer (100-μm pores). Cells were treated and analyzed according to the manufacturer's V3 library protocol (10x Genomics) and scRNA-seq at the next-generation sequencing core at the University of Pennsylvania. Data were analyzed using CellRanger v.6.1.2 and a pipeline that produced sparse numerical matrices for each sample, with gene-level counts of unique molecular identifiers (UMIs) identified for all single cells passing the default quality control metrics. These gene expression matrices were processed with the Seurat v.4.0 and Monocle 3 R packages[54]. For single-cell trajectory construction and pseudotime measurement, cells with an EC lineage were subsetted from the original dataset and then further reclustered and processed. Choice of root node was based on the local maximum of EC marker expression, which was determined by the spatial distribution of expressing cells and the gradient of expression.

Single-nucleus RNA-seq analysis. Cardiac tissues were excised from *Cdh5-Cre*^{ERT2};*Pdgfrb*$^{loxP/loxP}$ and *Pdgfrb*$^{loxP/loxP}$ mice, cut into small pieces and homogenized using a tissue grinder (catalog no. D8938; Sigma-Aldrich) in isolation buffer (0.32 M sucrose, 5 mM $CaCl_2$, 3 mM $MgAC_2$, 0.1 mM EDTA, 0.1% Triton X-100 and 10 mM Tris-HCl, pH 8.0) supplemented with cOmplete protease inhibitor cocktail (catalog no. 11697498001; Sigma-Aldrich). Tissues were processed with homogenizer pestle A for 15 strokes and homogenizer pestle B for 25 strokes to release the nuclei, followed by filtration with a 40-μm Flowmi cell strainer (catalog no. H13680-0040; SPBel-Art), centrifugation at 500*g* for 5 min at 4 °C and washing with 0.01% BSA in PBS. Nuclei were counted and diluted to 700–1,200 nuclei μl^{-1} and analyzed, followed by a 3′ GEX library protocol (V3.1; 10x Genomics) for single-nucleus RNA-seq at the next-generation sequencing core of the Children's Hospital of Philadelphia. Data were analyzed using CellRanger v.6.1.2 and a pipeline that produced sparse numerical matrices for each sample, with gene-level counts of UMIs identified for all single cells passing default quality control metrics. These gene expression matrices were processed with Seurat v.4.0 and Monocle 3 (ref. [54]).

Cardiac EC isolation, RNA amplification and RNA-seq analysis. MI or sham surgery were performed in 6–8-week-old *Tie2-Cre;Rosa-LSL-tdTomato* mice. Three weeks after the surgery, infarcted tissue or normal LV were collected. The single-cell suspension was prepared as described above. Cells were incubated with anti-F4/80 antibody (catalog no. 130-102-327; Miltenyi Biotec) and tdTomato^{+}F4/80^{-} cells were sorted with a flow cytometer (BD FACS Aria). RNA was extracted with TRIzol (catalog no. 15596026; Thermo Fisher Scientific) according to the manufacturer's instructions, followed by RNA purification using an RNeasy Plus Mini Kit (QIAGEN). Three-round mRNA amplification was performed as we described previously[55]. Briefly, complementary DNA was obtained by reverse transcription with SuperScript III (catalog no. 18080044; Thermo Fisher Scientific); a second complementary cDNA strand was synthesized by DNA polymerase (10 U μl^{-1}, catalog no. 18010025; Thermo Fisher Scientific), followed by in vitro RNA transcription with the MEGAscript T7 Kit (catalog no. AMB13345; Thermo Fisher Scientific) and RNA purification with the MEGAclear Kit (catalog no. AM1908; Thermo Fisher Scientific). After three rounds of mRNA amplification, quality control was validated using RNA Nano assay chips with a 2100 Bioanalyzer (Agilent Technologies). The library was constructed according to a TruSeq protocol (Agilent Technologies) followed by sequencing (100 PE, about 10-MB reads for each sample) with a HiSeq 2500 Illumina sequencer at the Children's Hospital of Philadelphia core facility.

Isolation and culture of mouse ECs. Mouse aorta ECs were isolated and cultured as we described previously[16]. Briefly, the thoracic aorta was isolated from three-week-old mice. The aortic rings were embedded in Matrigel-coated dishes and cultured for 5 d. After the rings were removed, the remaining cells were incubated with 2 U ml^{-1} Dispase I (catalog no. 17105-041; Gibco) for 20 min at 37 °C. After centrifugation at 500*g* for 10 min, the cell pellets were washed with PBS and cultured in EC medium (ECM) (catalog no. 1001; ScienCell).

Isolation and culture of mouse cardiomyocytes. Neonatal C57/B6 mouse pups (postnatal days 1–3) were euthanized. Hearts were excised and minced into small pieces in PBS supplemented with 20 mM BDM (catalog no. 31550; Merck Millipore) on ice, followed by digestion with 1.5 mg ml^{-1} collagenase/dispase enzyme mixture (catalog no. 10269638001; Sigma-Aldrich) in L-15 medium (catalog no. 11415064; Thermo Fisher Scientific) supplemented with 20 mM BDM at 37 °C for 30 min. The single-cell suspension was filtered with a 100-μm strainer, spun down at 300 r.p.m. for 5 min and resuspended in culture medium (L-15 medium supplemented with 10 mM HEPES and 5% FBS). After cells were incubated in a gelatin-coated culture dish at 37 °C for 3 h to allow cardiac fibroblasts and ECs to adhere to the culture dish, the supernatant was collected and cultured in a culture medium containing 10 μM Ara-C (catalog no. C6645; Sigma-Aldrich). Primary cardiomyocytes were cultured for 5–7 d with the medium changed every 3 d.

Tissue protein extraction. The heart tissues from *Cdh5-Cre*^{ERT2};*Pdgfrb*$^{loxP/loxP}$ and *Pdgfrb*$^{loxP/loxP}$ mice were collected and homogenized in PBS with proteinase inhibitor cocktail, followed by tissue lysis with NP-40 buffer.

Preparation of cardiac-conditioned medium. Mouse cardiac muscle HL-1 cells were cultured in Claycomb medium (catalog no. 51800C; Sigma-Aldrich) supplemented with 10% FBS (catalog no. F2442; Sigma-Aldrich), 0.1 mM norepinephrine (catalog no. A0937-1G; Sigma-Aldrich) and 2 mM L-Glutamine (catalog no. G7513; Sigma-Aldrich). Primary mouse cardiomyocytes were cultured in L-15 medium supplemented with 10 mM HEPES and 5% FBS. Cells at 90% confluence were exposed to hypoxia (1% O_2) or normoxia for 48 h. Mouse primary cardiac fibroblasts (ScienCell) were cultured in Claycomb medium. Culture medium was centrifuged at 5,000*g* for 30 min to remove cellular debris. Then, the supernatant was collected.

Cell culture and treatment. Human primary cardiac microvascular ECs (ScienCell and Cell Biologics) were maintained in ECM and used between passages 2 and 5. All cells were checked and showed no *Mycoplasma* contamination. Cells were treated with recombinant human PDGF-AA (100 ng ml^{-1}, catalog no. 100-13A; PeproTech), PDGF-AB (100 ng ml^{-1}, catalog no. 100-00AB; PeproTech), PDGF-BB (100 ng ml^{-1}, catalog no. 100-14B; PeproTech) or crenolanib (5 nM, catalog no. CP-868596; ChemieTek).

siRNA treatment. ECs at 50% confluence were transfected with control nontargeting siRNA (catalog no. 1027280; QIAGEN) or siRNAs targeting Snail (catalog no. s13185; Thermo Fisher Scientific), NF-κB (catalog no. 6261; Cell Signaling Technology), HIF1-α (catalog no. 42840; Thermo Fisher Scientific) or PDGFR-β (catalog no. s10242; Thermo Fisher Scientific) using Lipofectamine 2000 (catalog no. 11668-019; Thermo Fisher Scientific) in serum-free Opti-MEM medium (catalog no. 31985-070; Gibco) for 8 h, followed by recovery with serum-supplemented medium for 24 h.

CRISPR sgRNA treatment. Human primary cardiac ECs were treated with a dCas9 activation system (catalog nos. 61422 and 61426; Addgene) and a CDH5 SAM gRNA 5′-AGCCAGCCCAGCCCTCACAA-3′. ECs at 50% confluence were transduced with lentivirus encoding nontargeting control sgRNA or CDH5 SAM sgRNA with 8 μg ml^{-1} polybrene and spun at 2,000*g* for 2 h at room temperature. After centrifugation, cells were cultured in fresh ECM medium.

Cell viability assay. Treated ECs were trypsinized and seeded on 96-well plates at a density of 1,000 cells per well and allowed to attach for 4 h. Cell viability was determined by Cell-Titer assay (catalog no. G7571; Promega Corporation) according to the manufacturer's instructions. Luminescence was detected with a luminescent plate reader (Synergy H4 Hybrid; BioTek).

Cell migration assay. Treated ECs were seeded 5×10^4 cells per well on 8-μm pore insert membranes (catalog no. 353097; Falcon) in a 24-well plate and allowed to attach for 4 h. Cell migration was induced by adding 5% FBS to the bottom chamber. After a 4-h induction, cells on the top of the membrane were swiped off with cotton swabs. Cells were fixed in methanol for 10 min and stained with Toluidine Blue O (catalog no. 198161; Sigma-Aldrich) for 5 min. Images were taken in 3–4 fields for each well and stained cells were counted.

In vitro vascular permeability assay. Treated ECs were seeded on Transwell inserts with a 0.4-μm pore membrane (catalog no. 3413; Costar) in a 24-well plate and cultured overnight to reach confluence. Cells were incubated with ECM without phenol red. Fluorescein isothiocyanate (FITC)-dextran (molecular weight = 70,000 Da, 10 μg ml^{-1}, catalog no. SC-263323; Santa Cruz Biotechnology) was added to the top chamber. The medium from the lower chamber was collected and fluorescence was measured with the excitation wavelength at 485 nm and emission at 530 nm.

Dil-Ac-LDL absorption assay. Treated ECs were incubated with Dil-Ac-LDL (10 μg ml^{-1}, catalog no. J65597; Alfa Aesar) in serum-free medium containing 3% BSA for 5 h at 37 °C. Cells were fixed with 3% paraformaldehyde (PFA) and stained with anti-FSP1 antibody (1:100, catalog no. 07-2274; Merck Millipore) and Alexa Fluor 488-conjugated IgG. The slides were mounted with 4′,6-diamidino-2-phenylindole-containing mounting medium (catalog no. H-1200; Vector Laboratories) and imaged with an AxioImager microscope (ZEISS) equipped with an AxioCam 506 monochrome charge-coupled device (CCD) camera (ZEISS).

Immunoblot analysis. Cells were lysed with an NP-40 lysis buffer containing protease inhibitor cocktail, followed by measurement of total protein concentration. A total 20 μg lysate protein was resolved by 4–15% precast SDS–polyacrylamide gel electrophoresis (Bio-Rad Laboratories). After transfer, polyvinylidene difluoride membranes underwent immunoblotting with the following (obtained from Cell Signaling Technology unless stated otherwise): anti-glyceraldehyde-3-phosphate dehydrogenase (GAPDH) (catalog no. 5174); anti-FSP1; anti-VEGFR-2 (catalog no. 9698); anti-N-cadherin (catalog no. 13116); anti-α-SMA (catalog no. ab5694; Abcam); anti-NF-κB (catalog no. 8242); anti-Snail (catalog no. 3879S); anti-Slug (catalog no. 9585S); anti-TCF3 (catalog no. 2883); anti-ZEB1 (catalog no. 3396); anti-SIP1 (catalog no. A302-474A-T; Bethyl Laboratories); anti-HIF1-α (catalog no. 10006421; Cayman Chemical); anti-VE-cadherin (catalog no. 2500); anti-PDGFR-β (catalog no. 3169); anti-Akt (catalog no. 4685); anti-phospho-Akt (catalog no. 9271); anti-ERK1/2 (catalog no. 4695); and anti-phospho-ERK1/2 (catalog no. 4376) antibodies at 1:1,000 dilution. Proteins were detected with horseradish peroxidase-conjugated antibodies specific for either rabbit or mouse IgG (Bio-Rad Laboratories), followed by ECL development (catalog no. RPN2232; GE Healthcare).

Real-time RT–PCR analysis. Total RNA was extracted with TRIzol and underwent reverse transcription with the SuperScript III First-Strand Synthesis SuperMix (Thermo Fisher Scientific). Real-time PCR was performed in a 20-μl reaction volume using the Fast SYBR Green Master Mix (Applied Biosystems) and the following primers: HIF1A (forward: 5′-CATAAAGTCTGCAACATGGAAGGT-3′, reverse: 5′-ATTTGATGGGTGAGGAATGGGTT-3′); GAPDH (forward: 5′-GA GTCAACGGATTTGGTCGT-3′, reverse: 5′- GACAAGCTTCCCGTTCTCAG-3′).

Multiplex transcription factor activity analysis. ECs were starved in DMEM/F12 medium supplemented with 2% BSA overnight and treated with 100 ng ml^{-1} PDGF-AB under normoxia or 1% O_2 hypoxia for 6 h. The nuclear lysate was prepared with the NE-PER Nuclear and Cytoplasmic Extraction kit (catalog no. 78833; Thermo Fisher Scientific). Nuclear protein underwent transcriptional activity assay with a TF Activation Profiling Plate Array II kit (catalog no. FA-1002; Signosis) according to the manufacturer's instructions.

ChIP assay. Treated human cardiac microvascular ECs underwent ChIP analysis with a Magna ChIP Kit (catalog no. 17-610; Merck Millipore). Briefly, cells were fixed with 1% formaldehyde. Cells were scraped and lysed in nuclear buffer, followed by 6 cycles of continuous sonication for 8 × 2 s. Samples were incubated with anti-NF-κB (1:100), anti-HIF1-α (1:100, catalog no. 14179; Cell Signaling Technology) or anti-Snail (1:100, catalog no. AF3639; R&D Systems) antibody and with magnetic beads overnight at 4 °C. Normal IgG was used as the negative control. The immunoprecipitants were separated by magnetic rack and washed. The DNA fragments were released by incubation with proteinase K at 62 °C for 2 h. Real-time PCR was performed using Fast SYBR Green Master Mix with the following primers: NF-κB_Snail_FP, GTGTCCCTTTCCTCGCTTC; NF-κB_Snail_RP, GGTGGTCTGAGCGCTTCT; HIF1_Snail_FP no. 1, GGAGACGAGCCTC CGATT; HIF1_Snail_RP no. 1, GCCGCCAACTCCCTTAAGTA; HIF1_Snail_FP no. 2, GCGAGCTGCAGGACTCTAAT; HIF1_Snail_RP no. 2, GTGACTCGATCC TGGCTCA; Snail_Cdh5 FP no. 1, GGGTGGACAAGCACCTTAAA; Snail_Cdh5_RP no. 1, CAGCTCTGGGACTCTGAACC; Snail_Cdh5_FP no. 2, CCTCTGTGGA GACAGCCATC; Snail_Cdh5_RP no. 2, CTCCCCTTCAGGTTTTCCAG[41,44].

Immunofluorescence and histology. Mouse tissue sections and human cardiac specimens from healthy controls or individuals with MI (catalog no. MYO1301; BioCat) were deparaffinized and rehydrated, and underwent antigen retrieval in Target Retrieve Solution (catalog no. S1699; DAKO) at 95 °C for 20 min. Sections were blocked with 5% horse serum and incubated with anti-CD31 (1:100, catalog no. 3528, for human tissue; Cell Signaling Technology), anti-CD31 (1:100, catalog no. DIA-310, for mouse tissue; Dianova), anti-FSP1 (1:100), anti-α-SMA (1:100), anti-tropomyosin 1 (1:100, catalog no. ab55915; Abcam), anti-Snail (catalog no. MABE167; Merck Millipore), anti-collagen I (1:100, catalog no. MB176360; MyBioSource), anti-troponin T antibody (1:100, catalog no. MS295P1; Thermo Fisher Scientific), anti-PCNA (1:100, catalog no. sc-56; Santa Cruz Biotechnology)

or anti-vWF (1:100, catalog no. A0082; Dako) antibody overnight at 4 °C. For the TUNEL assay, sections were stained using a TUNEL kit (catalog no. C10617; Thermo Fisher Scientific) according to the manufacturer's protocol. For cell culture staining, cells were fixed with 4% PFA for 15 min and permeabilized with 1% Triton X-100 for 5 min. Cells were blocked with 5% horse serum for 1 h at room temperature and incubated with anti-FSP1 (1:100) overnight at 4 °C. Sections were stained with Alexa Fluor 488-, 568- or 647-conjugated secondary IgG (1:500; Thermo Fisher Scientific) for 1 h and Alexa Fluor 488-labeled phalloidin (1:100, catalog no. A12379; Invitrogen) for 20 min at room temperature. Images were acquired with an AxioImager microscope equipped with AxioCam 506 monochrome CCD camera and Zen v.2012 software (ZEISS). For the histological study, tissue sections were stained with Masson's trichrome dye and imaged with an AxioLab microscope (ZEISS) equipped with an AxioCam HRC CCD camera (ZEISS) and Zen software.

Measurement of MI size. MI size was measured as described previously[52]. Briefly, 28 d after LAD ligation, cardiac tissues were excised, embedded and serially cut at 8 µm from the apex to the level just below the coronary artery ligation site. Alternative sections were stained with Masson's trichrome dye. The infarcted area was measured by planimetry with ImageJ v.1.51 (National Institutes of Health (NIH)). Parameters were calculated using the equation: percentage infarct size = epicardial infarct length / epicardial LV circumference × 100.

Lectin perfusion and tissue clearing. MI or sham surgery was performed in 6–8-week-old mice. Mice were euthanized and perfused with 4% PFA in PBS. The normal or infarcted heart was collected and fixed in 4% PFA at 4 °C overnight. After PBS washing, the tissue was embedded in hydrogel solution. Tissue was cleared by electrophoresis at a 1.5-A current at 37 °C for 48 h or until visually clear in an X-CLARITY system according to a published protocol[56]. For lectin perfusion, anesthetized mice were administered DyLight 649-conjugated lectin (11 µg per mouse, catalog no. DL-1178; Vector Laboratories) via retro-orbital injection, followed by dye circulation for 5 min. After euthanasia, the mice chest cavity was opened, followed by transcardial perfusion and successively with 1% EDTA in PBS, 1% PFA, 10 µg ml^{-1} lectin in PBS for 3 min and 4% PFA. The hearts were excised, fixed in 4% PFA at 4 °C overnight and underwent tissue clearing.

Confocal imaging. After tissue clearing, 200-µm thick sections of normal or infarcted mouse heart was mounted in 88% Histodenz (catalog no. D2158; Sigma-Aldrich) in PBS-RIMS buffer with a refractive index of 1.46. Series of images within 100-µm depth were scanned by a TCS SP8 confocal microscope (Leica Microsystems). 3D images and movies were processed with the Imaris v.9.6 software and analyzed with the AngioTool v.0.5 software (NIH).

Light sheet fluorescence imaging. After tissue clearing, whole-heart tissue was immersed overnight in RIMS buffer with a refractive index of 1.46. Images were acquired with a Lightsheet Z.1 imager (ZEISS) at cell and developmental biology microscopy core at the University of Pennsylvania. 3D images and movies were processed and analyzed with Imaris v.9.6 software (Oxford Instruments).

SPECT. SPECT was performed with the MILabs U-SPECT+ system. Treated mice were injected intraperitoneally under anesthesia with ^{99m}Tc tetrofosmin (General Electric) according to the manufacturer's instructions, followed by SPECT scan at different layers. Images were analyzed with the AMIDE v.10.9 software.

Nanoparticle formulation and treatment. Polymer–lipid nanoparticles were generated as described previously[24,25]. Briefly, C15 alkyl epoxides were reacted with PEI_{600} at 90 °C in 100% ethanol for 48–72 h at a 14:1 molar ratio. The resulting compound was purified via high-performance liquid chromatography on a silica column in dichloromethane and then dissolved in 100% ethanol with a polyethylene glycol–lipid conjugate. In vivo siRNA targeting mouse PDGFR-β (catalog no. 4457302; Thermo Fisher Scientific) or a control sequence (catalog no. 4457289; Thermo Fisher Scientific) was dissolved in citrate buffer and then mixed in a microfluidic device with the previously described ethanol phase at a 2.5:1 flow rate ratio to form polymer–lipid nanoparticles[57]. Mice were underwent MI induction and were administered intraperitoneally with 1 mg kg^{-1} nanoparticles twice every week.

Statistics and reproducibility. An unpaired two-tailed Student's *t*-test (for two groups) and analysis of variance (ANOVA) (for more than two groups) were performed with Prism 9.3 (GraphPad Software) for statistical analyses between groups; $P < 0.05$ was considered to represent a statistically significant difference. No statistical method was used to predetermine sample size. The investigators were not blinded to allocation during the experiments and outcome assessment.

Reporting Summary. Further information on research design is available in the Nature Research Reporting Summary linked to this article.

Data availability

The RNA-seq data have been deposited in the National Center for Biotechnology Information's Gene Expression Omnibus under accession no. GSE163772, while the single-cell and single-nuclei RNA-seq analysis of mouse cardiac tissues with MI have been deposited in the same publicly available database under the accession nos. GSE163956 and GSE193290, respectively. The data supporting the findings of this study are available within the paper and its supplementary information. Source data are provided with this paper.

Received: 12 May 2021; Accepted: 7 March 2022;
Published online: 13 April 2022

References

1. Ware, J. A. & Simons, M. Angiogenesis in ischemic heart disease. *Nat. Med.* **3**, 158–164 (1997).
2. Harada, K. et al. Vascular endothelial growth factor administration in chronic myocardial ischemia. *Am. J. Physiol.* **270**, H1791–H1802 (1996).
3. Banai, S. et al. Angiogenic-induced enhancement of collateral blood flow to ischemic myocardium by vascular endothelial growth factor in dogs. *Circulation* **89**, 2183–2189 (1994).
4. Henry, T. D. et al. The VIVA trial: Vascular endothelial growth factor in Ischemia for Vascular Angiogenesis. *Circulation* **107**, 1359–1365 (2003).
5. Stewart, D. J. et al. VEGF gene therapy fails to improve perfusion of ischemic myocardium in patients with advanced coronary disease: results of the NORTHERN trial. *Mol. Ther.* **17**, 1109–1115 (2009).
6. Rajagopalan, S. et al. Regional angiogenesis with vascular endothelial growth factor in peripheral arterial disease: a phase II randomized, double-blind, controlled study of adenoviral delivery of vascular endothelial growth factor 121 in patients with disabling intermittent claudication. *Circulation* **108**, 1933–1938 (2003).
7. Potente, M., Gerhardt, H. & Carmeliet, P. Basic and therapeutic aspects of angiogenesis. *Cell* **146**, 873–887 (2011).
8. Goel, S. et al. Normalization of the vasculature for treatment of cancer and other diseases. *Physiol. Rev.* **91**, 1071–1121 (2011).
9. Kovacic, J. C., Mercader, N., Torres, M., Boehm, M. & Fuster, V. Epithelial-to-mesenchymal and endothelial-to-mesenchymal transition: from cardiovascular development to disease. *Circulation* **125**, 1795–1808 (2012).
10. Piera-Velazquez, S. & Jimenez, S. A. Endothelial to mesenchymal transition: role in physiology and in the pathogenesis of human diseases. *Physiol. Rev.* **99**, 1281–1324 (2019).
11. Zeisberg, E. M. et al. Endothelial-to-mesenchymal transition contributes to cardiac fibrosis. *Nat. Med.* **13**, 952–961 (2007).
12. Maddaluno, L. et al. EndMT contributes to the onset and progression of cerebral cavernous malformations. *Nature* **498**, 492–496 (2013).
13. Manavski, Y. et al. Clonal expansion of endothelial cells contributes to ischemia-induced neovascularization. *Circ. Res.* **122**, 670–677 (2018).
14. Li, Z. et al. Single-cell transcriptome analyses reveal novel targets modulating cardiac neovascularization by resident endothelial cells following myocardial infarction. *Eur. Heart J.* **40**, 2507–2520 (2019).
15. Tombor, L. S. et al. Single cell sequencing reveals endothelial plasticity with transient mesenchymal activation after myocardial infarction. *Nat. Commun.* **12**, 681 (2021).
16. Huang, M. et al. c-Met-mediated endothelial plasticity drives aberrant vascularization and chemoresistance in glioblastoma. *J. Clin. Invest.* **126**, 1801–1814 (2016).
17. Fan, Y. Vascular detransformation for cancer therapy. *Trends Cancer* **5**, 460–463 (2019).
18. De Palma, M. et al. Tie2 identifies a hematopoietic lineage of proangiogenic monocytes required for tumor vessel formation and a mesenchymal population of pericyte progenitors. *Cancer Cell* **8**, 211–226 (2005).
19. Andrae, J., Gallini, R. & Betsholtz, C. Role of platelet-derived growth factors in physiology and medicine. *Genes Dev.* **22**, 1276–1312 (2008).
20. Acloque, H., Adams, M. S., Fishwick, K., Bronner-Fraser, M. & Nieto, M. A. Epithelial-mesenchymal transitions: the importance of changing cell state in development and disease. *J. Clin. Invest.* **119**, 1438–1449 (2009).
21. Kalluri, R. & Weinberg, R. A. The basics of epithelial-mesenchymal transition. *J. Clin. Invest.* **119**, 1420–1428 (2009).
22. Lamouille, S., Xu, J. & Derynck, R. Molecular mechanisms of epithelial–mesenchymal transition. *Nat. Rev. Mol. Cell Biol.* **15**, 178–196 (2014).
23. Liu, T. et al. PDGF-mediated mesenchymal transformation renders endothelial resistance to anti-VEGF treatment in glioblastoma. *Nat. Commun.* **9**, 3439 (2018).
24. Khan, O. F. et al. Endothelial siRNA delivery in nonhuman primates using ionizable low-molecular weight polymeric nanoparticles. *Sci. Adv.* **4**, eaar8409 (2018).
25. Krohn-Grimberghe, M. et al. Nanoparticle-encapsulated siRNAs for gene silencing in the haematopoietic stem-cell niche. *Nat. Biomed. Eng.* **4**, 1076–1089 (2020).
26. Hoeben, A. et al. Vascular endothelial growth factor and angiogenesis. *Pharmacol. Rev.* **56**, 549–580 (2004).

27. Forsythe, J. A. et al. Activation of vascular endothelial growth factor gene transcription by hypoxia-inducible factor 1. *Mol. Cell. Biol.* **16**, 4604–4613 (1996).
28. Oladipupo, S. et al. VEGF is essential for hypoxia-inducible factor-mediated neovascularization but dispensable for endothelial sprouting. *Proc. Natl Acad. Sci. USA* **108**, 13264–13269 (2011).
29. Nagy, J. A., Dvorak, A. M. & Dvorak, H. F. VEGF-A and the induction of pathological angiogenesis. *Annu. Rev. Pathol.* **2**, 251–275 (2007).
30. Carmeliet, P. & Jain, R. K. Principles and mechanisms of vessel normalization for cancer and other angiogenic diseases. *Nat. Rev. Drug Discov.* **10**, 417–427 (2011).
31. Potenta, S., Zeisberg, E. & Kalluri, R. The role of endothelial-to-mesenchymal transition in cancer progression. *Br. J. Cancer* **99**, 1375–1379 (2008).
32. Chen, P.-Y. et al. Endothelial-to-mesenchymal transition drives atherosclerosis progression. *J. Clin. Invest.* **125**, 4514–4528 (2015).
33. Dejana, E., Hirschi, K. K. & Simons, M. The molecular basis of endothelial cell plasticity. *Nat. Commun.* **8**, 14361 (2017).
34. Thiery, J. P. Epithelial–mesenchymal transitions in tumour progression. *Nat. Rev. Cancer* **2**, 442–454 (2002).
35. Peinado, H., Olmeda, D. & Cano, A. Snail, Zeb and bHLH factors in tumour progression: an alliance against the epithelial phenotype? *Nat. Rev. Cancer* **7**, 415–428 (2007).
36. Nieto, M. A. The snail superfamily of zinc-finger transcription factors. *Nat. Rev. Mol. Cell Biol.* **3**, 155–166 (2002).
37. Bachelder, R. E., Yoon, S.-O., Franci, C., de Herreros, A. G. & Mercurio, A. M. Glycogen synthase kinase-3 is an endogenous inhibitor of Snail transcription: implications for the epithelial–mesenchymal transition. *J. Cell Biol.* **168**, 29–33 (2005).
38. Pires, B. R. B. et al. NF-kappaB is involved in the regulation of EMT genes in breast cancer cells. *PLoS ONE* **12**, e0169622 (2017).
39. Zhu, Y. et al. HIF-1α regulates EMT via the Snail and β-catenin pathways in paraquat poisoning-induced early pulmonary fibrosis. *J. Cell. Mol. Med.* **20**, 688–697 (2016).
40. Zhang, L. et al. Hypoxia induces epithelial-mesenchymal transition via activation of SNAI1 by hypoxia-inducible factor-1α in hepatocellular carcinoma. *BMC Cancer* **13**, 108 (2013).
41. Xu, X. et al. Snail is a direct target of hypoxia-inducible factor 1α (HIF1α) in hypoxia-induced endothelial to mesenchymal transition of human coronary endothelial cells. *J. Biol. Chem.* **290**, 16653–16664 (2015).
42. Kokudo, T. et al. Snail is required for TGFβ-induced endothelial-mesenchymal transition of embryonic stem cell-derived endothelial cells. *J. Cell Sci.* **121**, 3317–3324 (2008).
43. Mahmoud, M. M. et al. Shear stress induces endothelial-to-mesenchymal transition via the transcription factor Snail. *Sci. Rep.* **7**, 3375 (2017).
44. Cheng, J.-C., Chang, H.-M. & Leung, P. C. K. Transforming growth factor-β1 inhibits trophoblast cell invasion by inducing Snail-mediated down-regulation of vascular endothelial-cadherin protein. *J. Biol. Chem.* **288**, 33181–33192 (2013).
45. Lopez, D., Niu, G., Huber, P. & Carter, W. B. Tumor-induced upregulation of Twist, Snail, and Slug represses the activity of the human VE-cadherin promoter. *Arch. Biochem. Biophys.* **482**, 77–82 (2009).
46. Ishikawa, F. et al. Identification of angiogenic activity and the cloning and expression of platelet-derived endothelial cell growth factor. *Nature* **338**, 557–562 (1989).
47. Benjamin, L. E., Hemo, I. & Keshet, E. A plasticity window for blood vessel remodelling is defined by pericyte coverage of the preformed endothelial network and is regulated by PDGF-B and VEGF. *Development* **125**, 1591–1598 (1998).
48. Battegay, E. J., Rupp, J., Iruela-Arispe, L., Sage, E. H. & Pech, M. PDGF-BB modulates endothelial proliferation and angiogenesis in vitro via PDGF beta-receptors. *J. Cell Biol.* **125**, 917–928 (1994).
49. Liu, C. et al. Platelet-derived growth factor blockade on cardiac remodeling following infarction. *Mol. Cell. Biochem.* **397**, 295–304 (2014).
50. Zymek, P. et al. The role of platelet-derived growth factor signaling in healing myocardial infarcts. *J. Am. Coll. Cardiol.* **48**, 2315–2323 (2006).
51. Wang, Y. et al. Ephrin-B2 controls VEGF-induced angiogenesis and lymphangiogenesis. *Nature* **465**, 483–486 (2010).
52. Gong, Y., Zhao, Y., Li, Y., Fan, Y. & Hoover-Plow, J. Plasminogen regulates cardiac repair after myocardial infarction through its noncanonical function in stem cell homing to the infarcted heart. *J. Am. Coll. Cardiol.* **63**, 2862–2872 (2014).
53. Lang, R. M. et al. Recommendations for cardiac chamber quantification by echocardiography in adults: an update from the American Society of Echocardiography and the European Association of Cardiovascular Imaging. *Eur. Heart J. Cardiovasc. Imaging* **16**, 233–270 (2015).
54. Qiu, X. et al. Single-cell mRNA quantification and differential analysis with Census. *Nat. Methods* **14**, 309–315 (2017).
55. Liu, T. et al. Circulating glioma cells exhibit stem cell-like properties. *Cancer Res.* **78**, 6632–6642 (2018).
56. Yang, B. et al. Single-cell phenotyping within transparent intact tissue through whole-body clearing. *Cell* **158**, 945–958 (2014).
57. Billingsley, M. M. et al. Ionizable lipid nanoparticle-mediated mRNA delivery for human CAR T cell engineering. *Nano Lett.* **20**, 1578–1589 (2020).

Acknowledgements

We thank J. Eberwine (Penn Pharmacology), J. Schug (Penn Next-Generation Sequencing Core), A. Stout (Penn CDB Microscope Core) and E. Blankemeyer (Penn Small Animal Imaging Core) for assistance with RNA linear amplification, scRNA-seq, light sheet fluorescence imaging and SPECT analysis, respectively. This work was supported in part by an American Heart Association (AHA) Innovative Project Award no. IPA34170252 (to Y.F.), National Institutes of Health (NIH) grant nos. R01HL155198 (to Y.F. and Y.G.) and R01NS094533, R01NS106108 and R01CA241501 (to Y.F.), American Association for Cancer Research (AACR) Judah Folkman Award (to Y.F.), AHA Scientist Development grant no. SDG9050018 and grant-in-Aid no. GRNT3365002 (to Y.G.) and AHA Predoctoral Fellowship (to D.Z.). L.P. is supported by the Office of the Assistant Secretary of Defense for Health Affairs through the Peer Reviewed Medical Research Program (nos. W81XWH2010042 and W81XWH2010089). M.J.M. acknowledges support from a Burroughs Wellcome Fund Career Award at the Scientific Interface, an NIH Director's New Innovator Award (no. DP2 TR002776), NIH grant nos. R01CA241661, R37CA244911 and R01DK123049, an Abramson Cancer Center-School of Engineering and Applied Sciences Discovery Grant (no. P30CA016520) and an AACR-Bayer Innovation and Discovery Grant (no. 18-80-44-MITC).

Author contributions

M.H., F.Y., D.Z. and M.L. designed, performed and analyzed the experiments. D.Z., L.Z. and L.Q. contributed to the scRNA-seq studies. M.L. and S.V.S. contributed to the echocardiogram analysis. H.D. helped tissue histology analysis. R.E. and M.J.M. contributed to nanoparticle production. L.P. helped with the single-nucleus analysis. D.J.R. contributed to the experimental design and discussion. Y.G. and M.L. performed the MI surgery. Y.F. and Y.G. cosupervised the experiments and wrote the manuscript. All authors commented on the manuscript.

Competing interests

The authors declare no competing interests.

Additional information

Extended data is available for this paper at https://doi.org/10.1038/s44161-022-00047-3.

Supplementary information The online version contains supplementary material available at https://doi.org/10.1038/s44161-022-00047-3.

Correspondence and requests for materials should be addressed to Yi Fan or Yanqing Gong.

Peer review information *Nature Cardiovascular Research* thanks the anonymous reviewers for their contribution to the peer review of this work.

Reprints and permissions information is available at www.nature.com/reprints.

Publisher's note Springer Nature remains neutral with regard to jurisdictional claims in published maps and institutional affiliations.

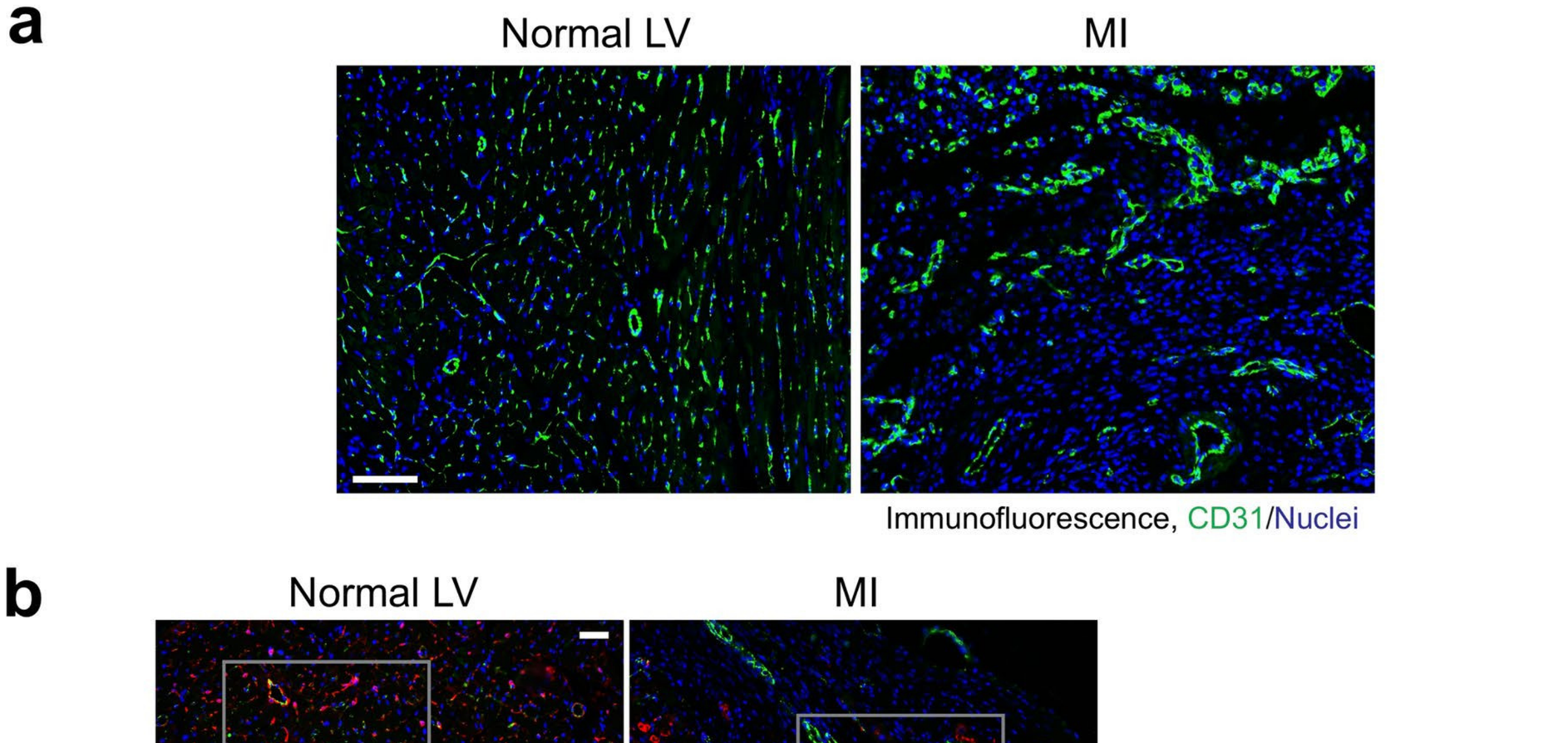

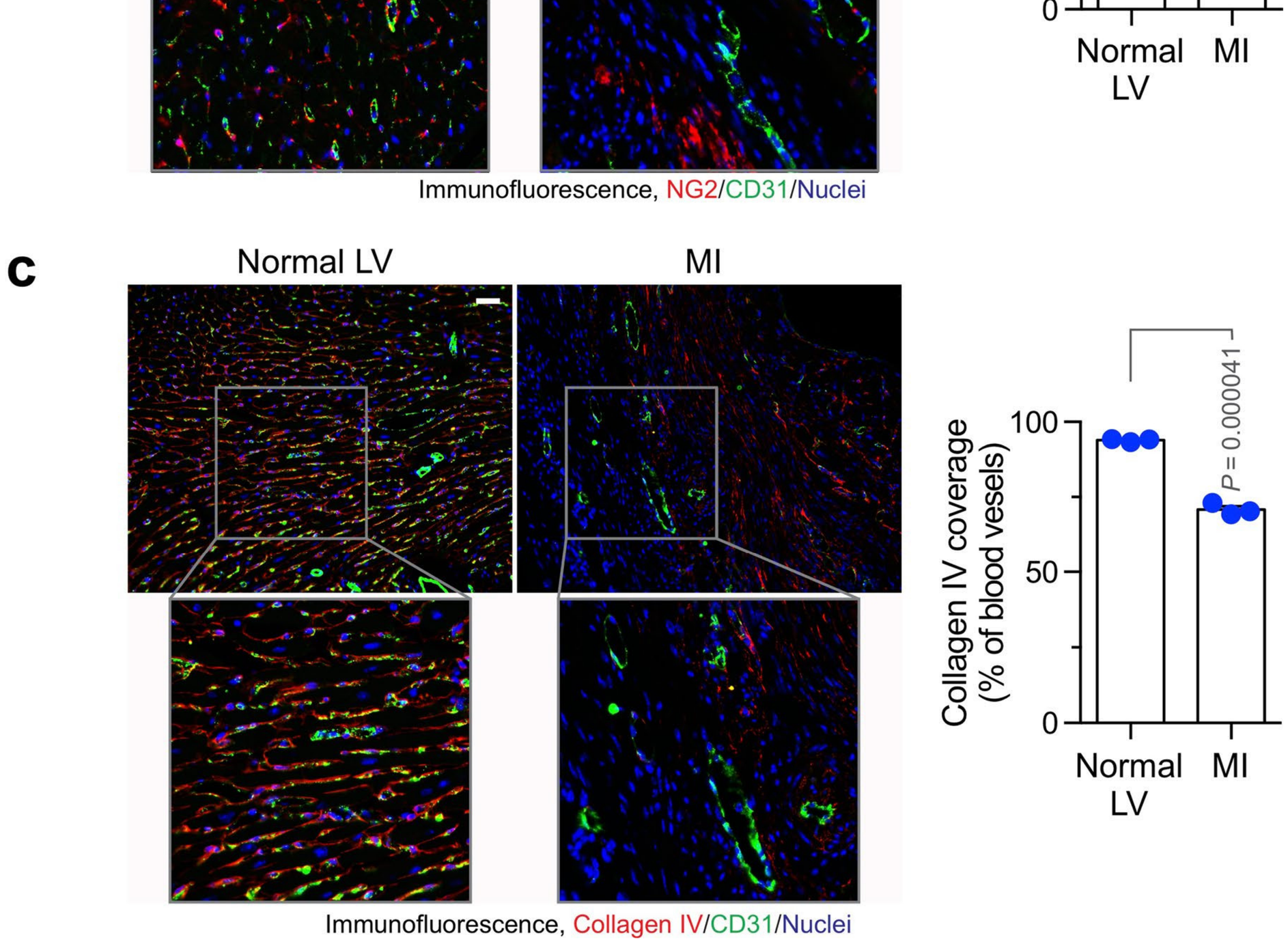

Extended Data Fig. 1 | See next page for caption.

Extended Data Fig. 1 | Aberrant vascularization characterizes infarcted cardiac tissue. Mice were subjected to MI surgery or sham operation. Hearts were excised 3 weeks after surgery. Tissue sections were immunostained with (**a**) anti-CD31 antibody, (**b**) anti-NG2 and anti-CD31 antibodies, or (**c**) anti-collagen IV and anti-CD31 antibodies. **a**, Representative images in normal tissue and infarct zone are shown (n = 3 mice). Bars indicate 100 μm. **b**,**c**, Left, representative images in normal tissue and infarct zone are shown. Right, quantified results (mean ± SEM, n = 3 mice). Statistical analysis by unpaired two-tailed Students' t test. Bars indicate 100 μm.

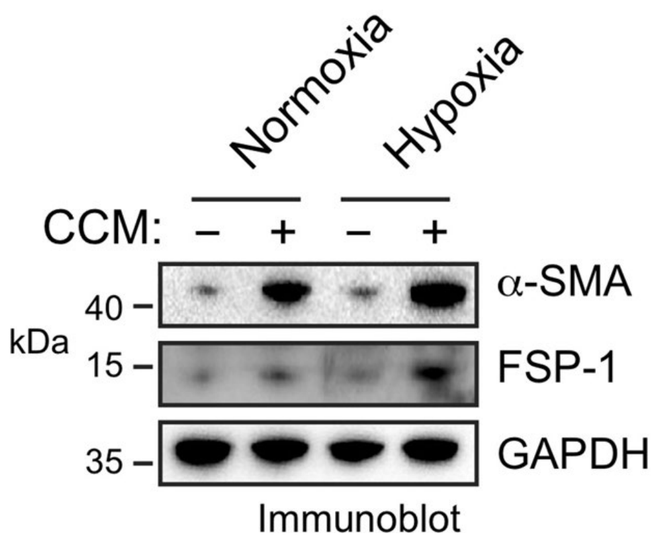

Extended Data Fig. 2 | Cardiomyocyte-conditioned medium induces FSP-1 and α-SMA expression in ECs. Mouse cardiac-conditioned medium (CCM) were harvested from primary mouse cardiomyocytes cultured under hypoxia (1% O_2). Mouse cardiac microvascular ECs were treated with CCM under normoxia or hypoxia for 2 days. Cell lysates were immunoblotted. These experiments were repeated independently twice with similar results.

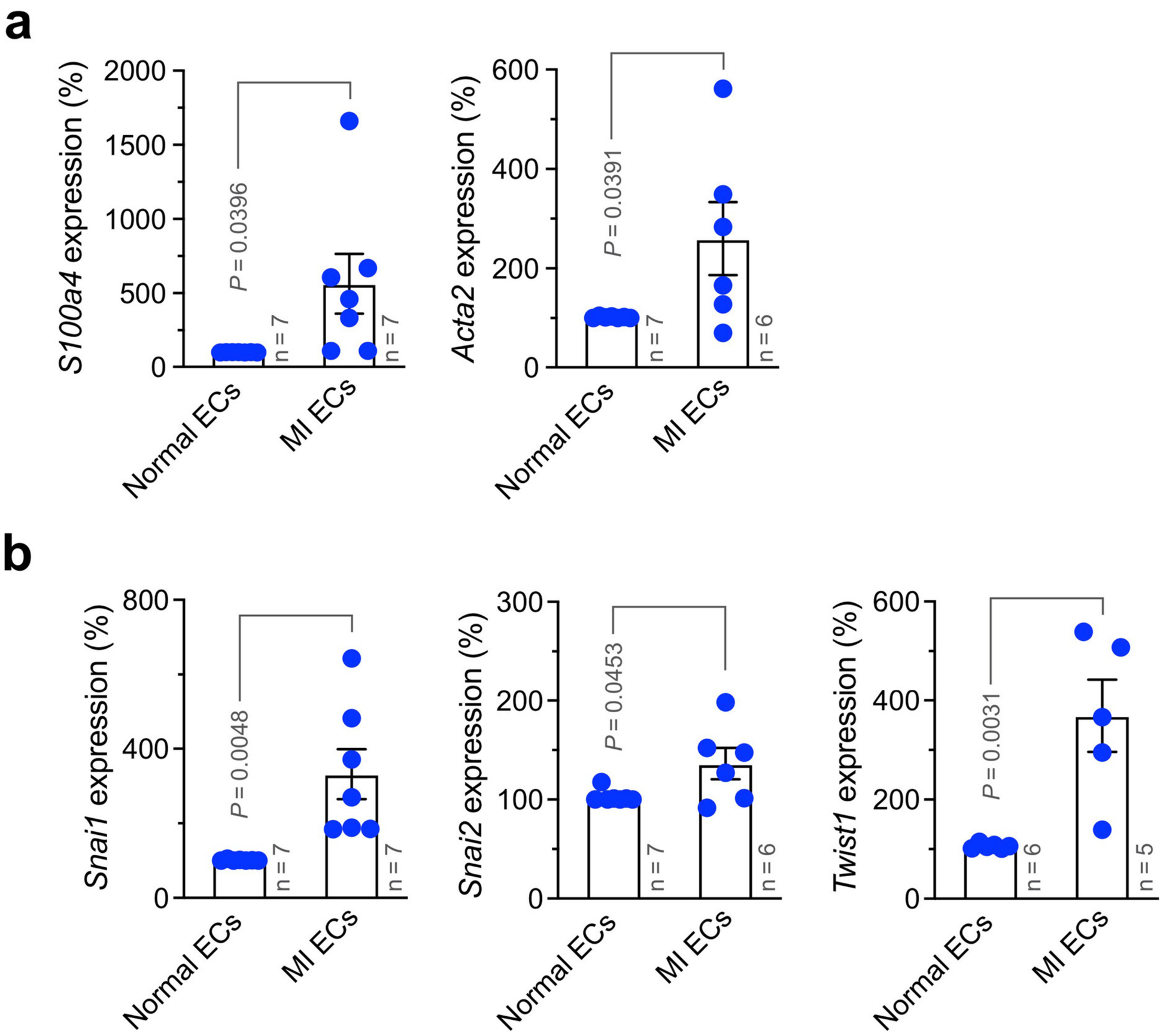

Extended Data Fig. 3 | Expression of mesenchymal genes in MI-associated ECs. MI was induced in wild-type mice. Three weeks after MI induction, ECs were isolated from normal LV and MI tissues. RNA was extracted and subjected to RT-PCR analysis (mean ± SEM, n = 5-7 mice, specific n indicated in the graphs). Statistical analysis by unpaired two-tailed Students' t test. Expression of (**a**) S100A4 (FSP-1) and Acta2 (α-SMA), and (**b**) Snai1 (Snail), Snai2 (Slug), and Twist1 was normalized with GAPDH expression levels.

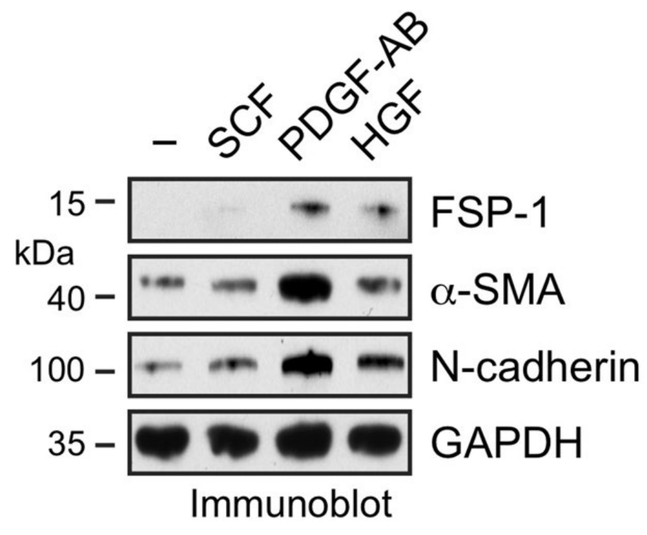

Extended Data Fig. 4 | PDGF-AB induces expression of mesenchymal proteins in ECs. Human cardiac microvascular ECs were treated with 100 ng/ml SCF, PDGF-AB, or HGF for 2 days under hypoxia. Cell lysates were immunoblotted. These experiments were repeated independently twice with similar results.

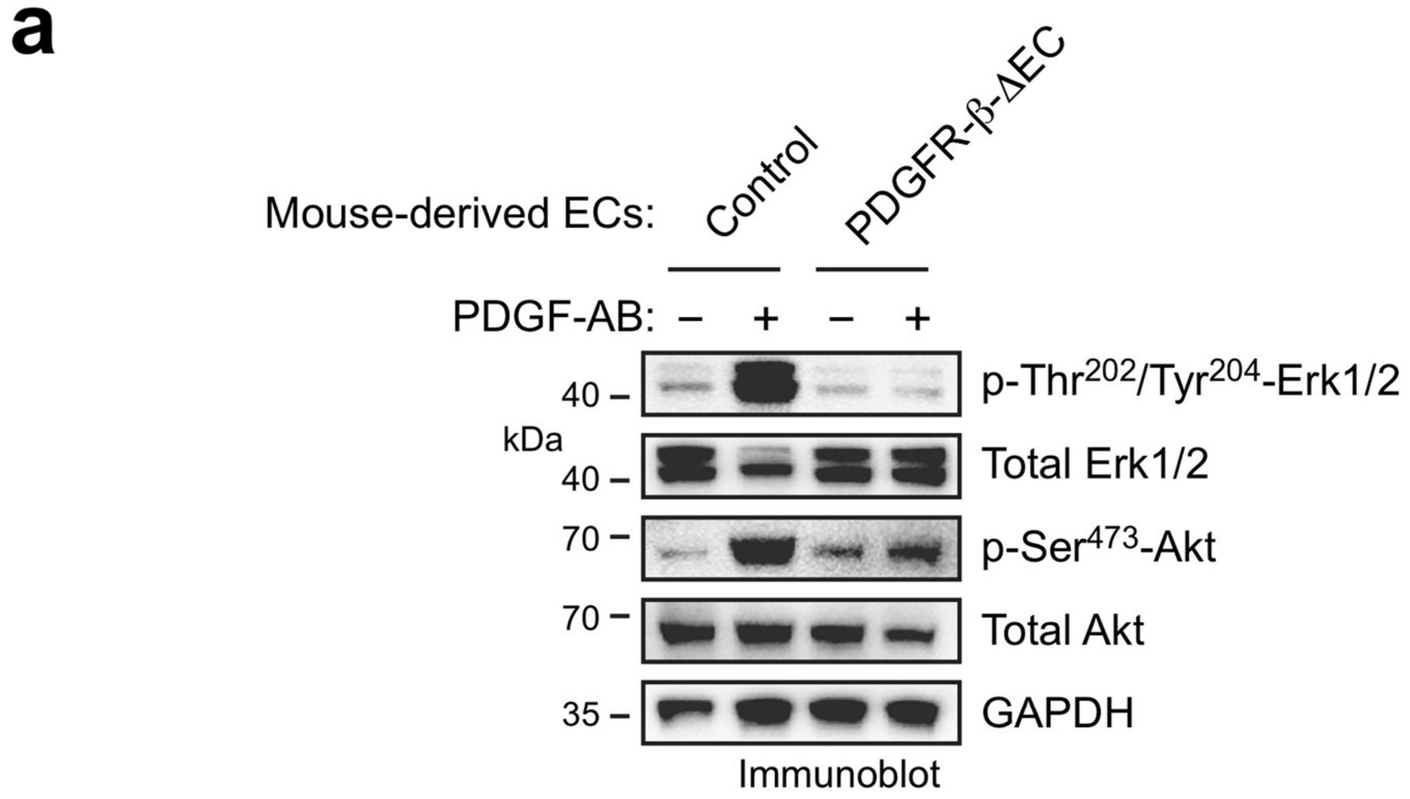

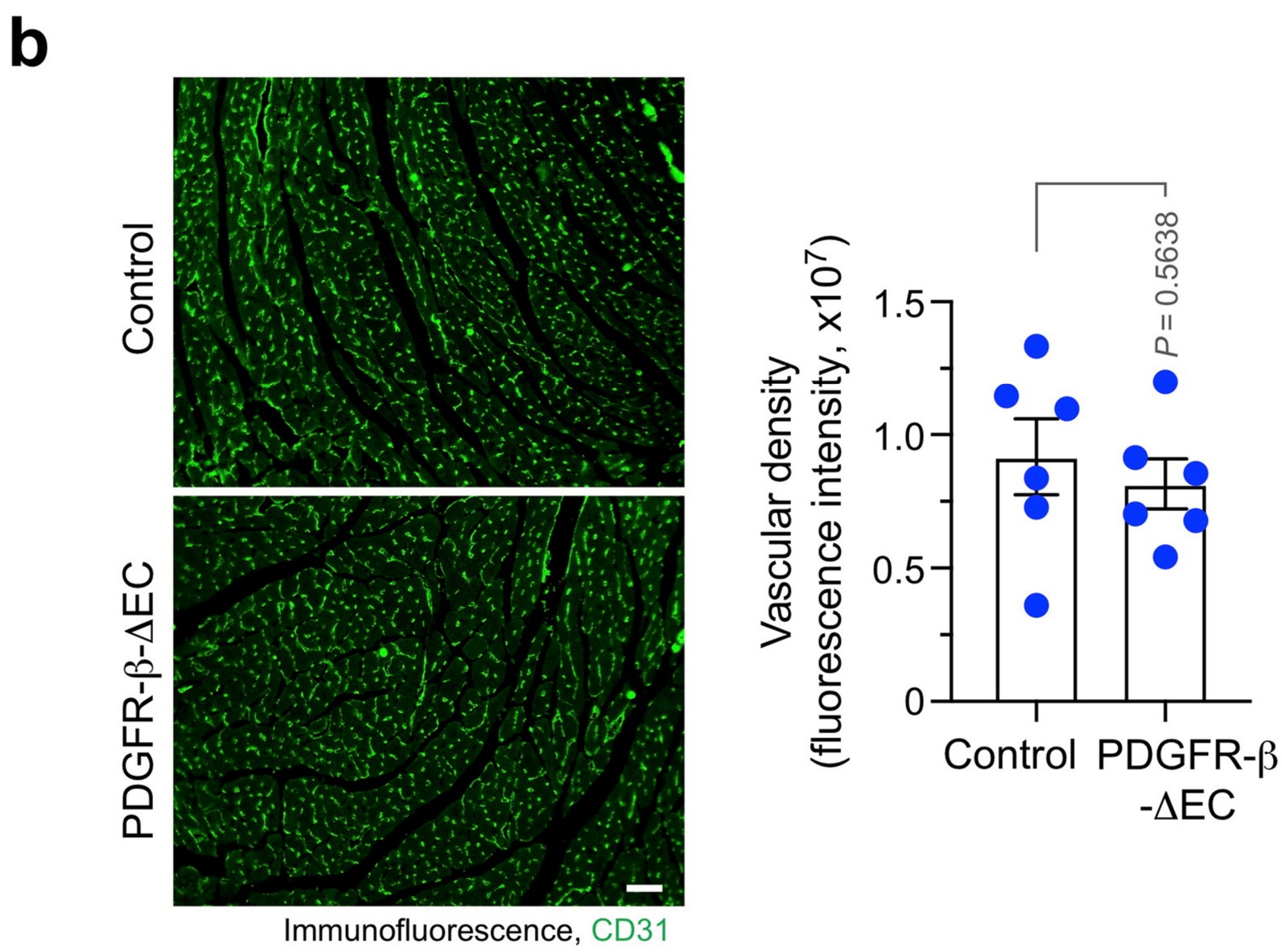

Extended Data Fig. 5 | PDGFR-β knockout inhibits PDGF-AB-induced phosphorylation of Erk1 and Akt1 in ECs and does not affect vascular density in normal hearts. a, Aortic ECs were isolated from tamoxifen-treated *Cdh5-Cre*^{ERT2};*Pdgfrb*$^{fl/fl}$ (PDGFR-β-ΔEC) and *Pdgfrb*$^{fl/fl}$ (control) mice. Cells were treated with 100 ng/ml PDGF-AB for 10 min, followed by immunoblot analysis. These experiments were repeated independently twice with similar results. **b**,Left ventricles were collected from PDGFR-β-ΔEC and control mice. Cardiac sections were stained with anti-CD31 antibody and analyzed by immunofluorescence. Left, representative images are shown. Scale bar: 200 μm. Right, quantified results (mean ± SEM, n = 6 mice). Statistical analysis by unpaired two-tailed Students' t test.

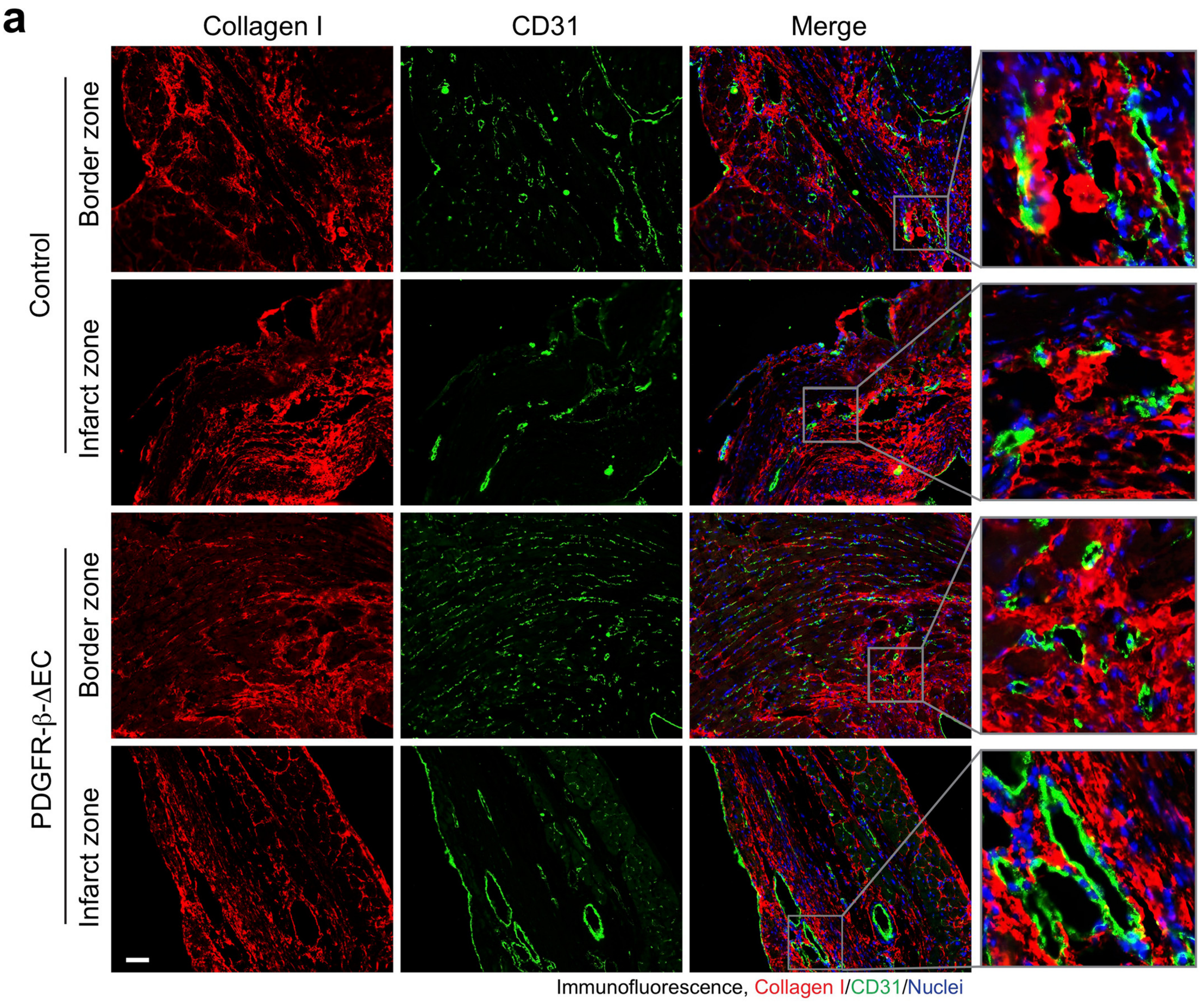

Extended Data Fig. 6 | PDGFR-β knockout in ECs does not increase vascular density in infarct zone and border zone. MI was induced in control and PDGFR-β-ΔEC mice. (**a**,**b**) 4 or (**c**) 8 weeks after MI induction, cardiac tissues were collected. Sections were stained with anti-collagen I and anti-CD31 antibodies, followed by immunofluorescence analysis. **a**, Representative images are shown (n = 6 mice). Scale bar: 100 μm. **b**,**c**, Vascular density was quantified (mean ± SEM). **b**, n = 3-4 mice, specific n indicated in the graphs. **c**, n = 6 mice. Statistical analysis by two-way ANOVA Fisher's test.

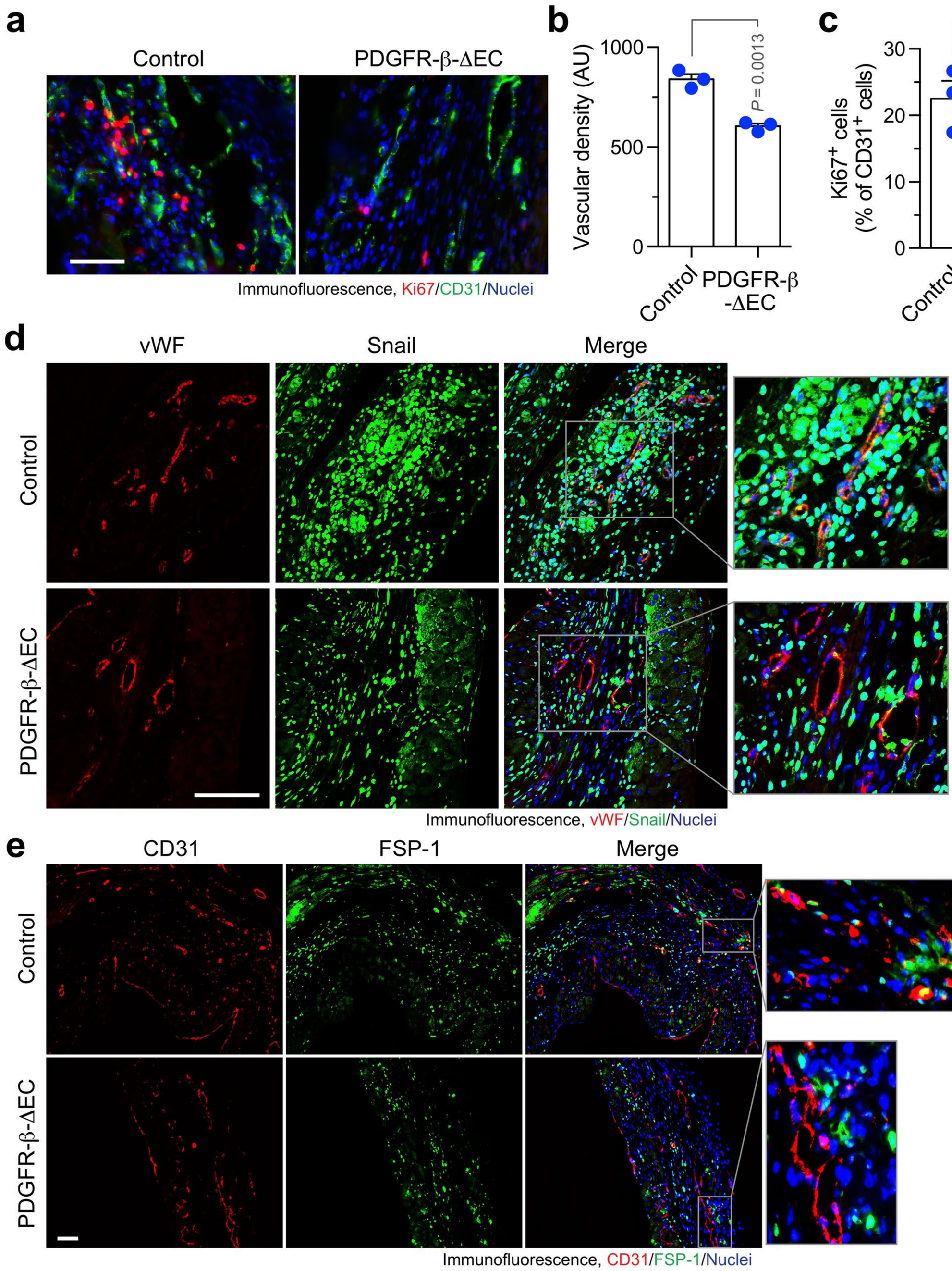

Extended Data Fig. 7 | PDGFR-β knockout reduces vascular density and inhibits Ki67, Snail and FSP-1 expression in MI- associated ECs. MI was induced in WT and PDGFR-β-ΔEC mice. Hearts were excised 3 weeks after surgery. MI tissue sections were immunostained with (**a**-**c**) anti-Ki67 and anti-CD31, (**d**) anti-vWF and anti-Snail, or (**e**) anti-CD31 and anti-FSP-1 antibodies. **a**, Representative immunofluorescence images in infarct zone are shown (n = 3 mice). Scale bar: 100 μm. **b**,**c**, quantified results (mean ± SEM, n = 3 mice). **b**, Density of $CD31^+$ cells. AU, arbitrary unit. **c**, Ki67 expression in $CD31^+$ cells. Statistical analysis by unpaired two-tailed Students' t test. **d**,**e**, Representative immunofluorescence images in infarct zone are shown (n = 5 mice). Scale bar: 100 μm.

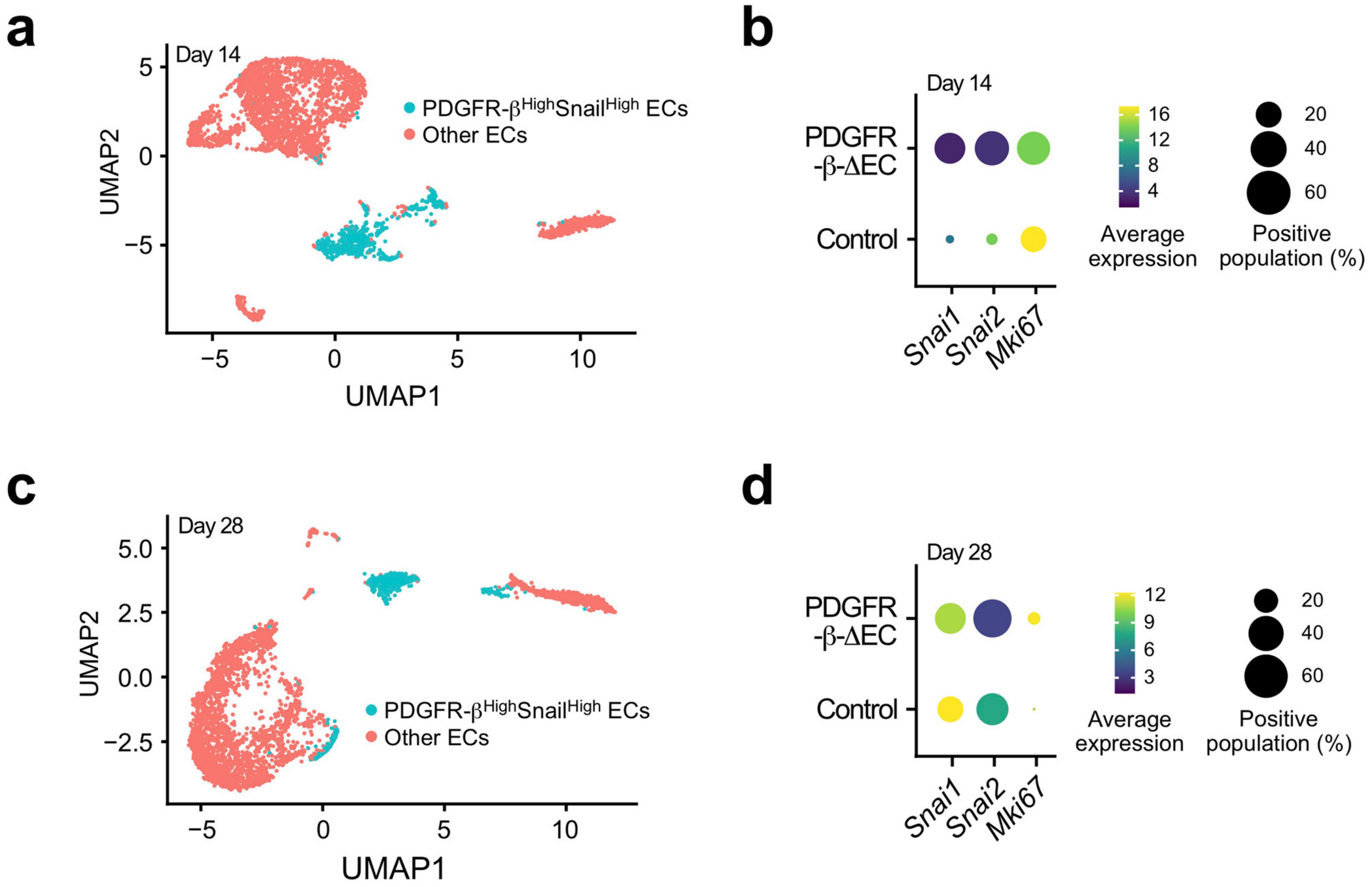

Extended Data Fig. 8 | PDGFR-β knockout reduces Snail expression in MI-associated ECs. MI was induced in WT and PDGFR-β-ΔEC mice. (**a**,**b**) 14 and (**c**,**d**) 28 days after MI induction, MI tissue sections were collected and subjected to single-nuclei RNA sequencing analysis (total = 4 mice). Uniform manifold approximation and projection (UMAP) analysis of transcriptome gene signature in ECs. (**a**,**c**) UMAP analysis of ECs. (**b**,**d**) Expression of Snail, Slug, and Ki67 in ECs.

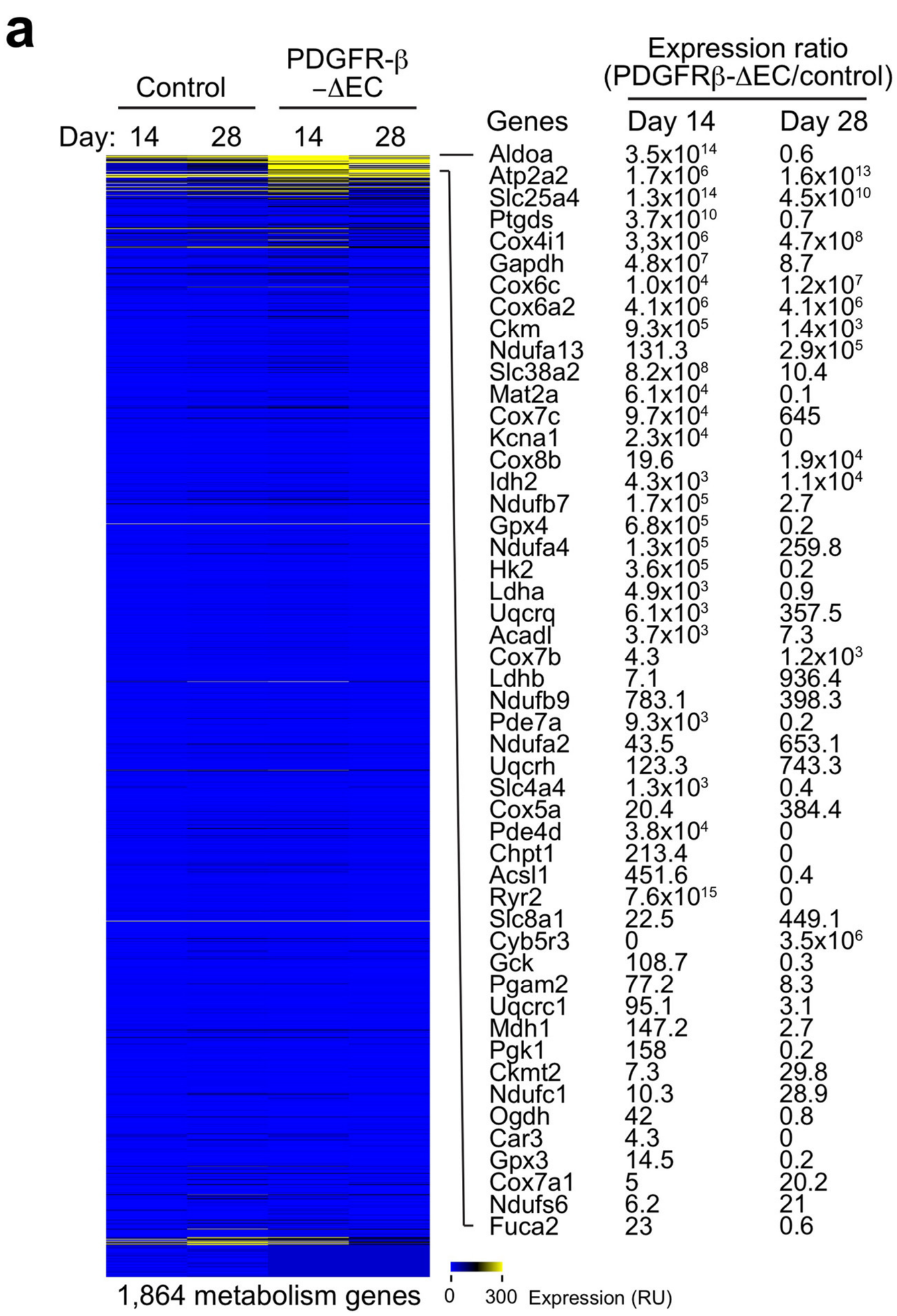

Extended Data Fig. 9 | PDGFR-β knockout in ECs alters expression of metabolism-associated genes in myocytes. MI was induced in WT and PDGFR-β-ΔEC mice. 14 and 28 days after MI induction, MI tissue sections were collected and subjected to single-nuclei RNA sequencing analysis (total = 4 mice). Expression of metabolism-associated genes were analyzed. **a**, Heatmap of mapped genes. **b**, Global changes in gene expression at days 14 and 28 after MI induction.

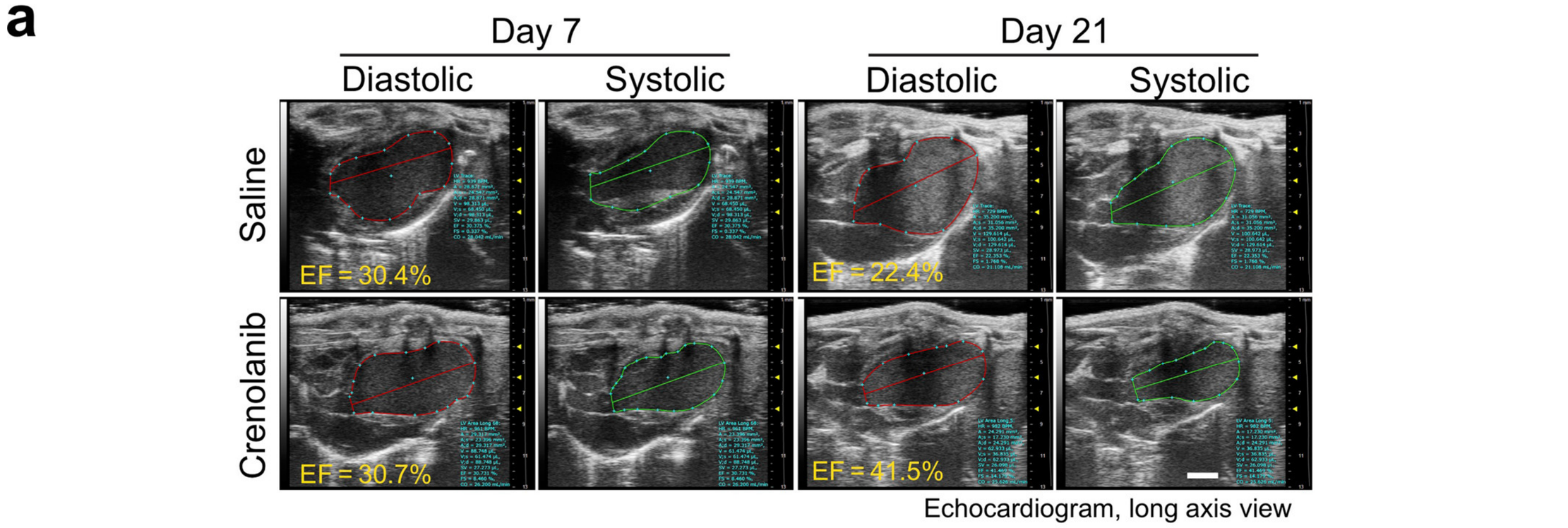

Extended Data Fig. 10 | PDGFR inhibition improves cardiac function recovery and promotes tissue repair after MI. MI was induced in mice, followed by administration with saline or 15 mg/kg crenolanib. **a**,**b**, Cardiac function was analyzed by echocardiogram (n = 11 mice). Representative images are shown. **a**, Long-axis echocardiogram analysis. Scale bar: 2 mm. **b**, M mode echocardiogram analysis. Scale bar: 2 mm. Arrows indicate myocardial anterior walls. **c**,**d**, Heart tissues were harvested 3 weeks after MI induction. Cardiac sections were stained with Masson's trichrome stain. **c**, Representative images are shown (n = 4 mice). Scale bar: 500 μm. Arrows indicate epicardium. **d**, Quantified cardiomyocyte area (mean ± SEM, n = 4-5 mice). Statistical analysis by unpaired two-tailed Students' t test. **e**, Heart tissues were harvested 3 weeks after MI induction. Cardiac sections were stained with an anti-CD31 antibody and analyzed by immunofluorescence imaging. Vascular density was quantified (mean ± SEM, n = 5 mice). Statistical analysis by two-way ANOVA.

nature research

Corresponding author(s): Yi Fan, Yanqing Gong

Last updated by author(s): Mar 3, 2022

Reporting Summary

Nature Research wishes to improve the reproducibility of the work that we publish. This form provides structure for consistency and transparency in reporting. For further information on Nature Research policies, see our Editorial Policies and the Editorial Policy Checklist.

Statistics

For all statistical analyses, confirm that the following items are present in the figure legend, table legend, main text, or Methods section.

n/a	Confirmed	
☐	☒	The exact sample size (*n*) for each experimental group/condition, given as a discrete number and unit of measurement
☐	☒	A statement on whether measurements were taken from distinct samples or whether the same sample was measured repeatedly
☐	☒	The statistical test(s) used AND whether they are one- or two-sided *Only common tests should be described solely by name; describe more complex techniques in the Methods section.*
☒	☐	A description of all covariates tested
☐	☒	A description of any assumptions or corrections, such as tests of normality and adjustment for multiple comparisons
☐	☒	A full description of the statistical parameters including central tendency (e.g. means) or other basic estimates (e.g. regression coefficient) AND variation (e.g. standard deviation) or associated estimates of uncertainty (e.g. confidence intervals)
☐	☒	For null hypothesis testing, the test statistic (e.g. *F*, *t*, *r*) with confidence intervals, effect sizes, degrees of freedom and *P* value noted *Give P values as exact values whenever suitable.*
☒	☐	For Bayesian analysis, information on the choice of priors and Markov chain Monte Carlo settings
☒	☐	For hierarchical and complex designs, identification of the appropriate level for tests and full reporting of outcomes
☒	☐	Estimates of effect sizes (e.g. Cohen's *d*, Pearson's *r*), indicating how they were calculated

Our web collection on statistics for biologists contains articles on many of the points above.

Software and code

Policy information about availability of computer code

Data collection	Zeiss Zen for microscopy imaging. Illumina sequencer HiSeq 2500 for RNAseq data.
Data analysis	Graphpad Prism 9.3 for statistical analysis. CellRanger software 6.1.2, Seurat 4.0, and Monocle3 R package for single-cell and single-nuclei RNAseq analyses. ImageJ 1.51 with AngioTool software for image analysis. FlowJo v9 for flow cytometry sorting data analysis. Arivis 4D (Arivis AG) and Imaris 9.6 (Oxford Instruments) for 3-D image analysis. Vevo Lab 3.2.0 software (VisualSonics) for cardiac function analysis. AMIDE 10.9 for SPECT data analysis.

For manuscripts utilizing custom algorithms or software that are central to the research but not yet described in published literature, software must be made available to editors and reviewers. We strongly encourage code deposition in a community repository (e.g. GitHub). See the Nature Research guidelines for submitting code & software for further information.

Data

Policy information about availability of data

All manuscripts must include a data availability statement. This statement should provide the following information, where applicable:

- Accession codes, unique identifiers, or web links for publicly available datasets
- A list of figures that have associated raw data
- A description of any restrictions on data availability

Single-cell, single-nuclei, and bulk RNA-seq data have been deposited in NCBI's Gene Expression Omnibus under accession (GSE163956, GSE163772, and